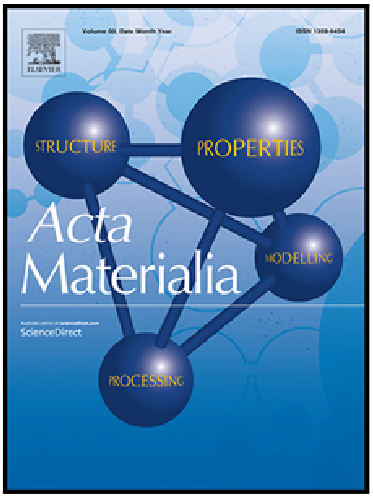

On the impact of the mesostructure on the creep response of cellular NiAl-Mo eutectics

Daniel Wicht, Alexander Kauffmann, Matti Schneider,
Martin Heilmaier, Thomas Böhlke

PII: S1359-6454(22)00010-6
DOI: https://doi.org/10.1016/j.actamat.2022.117626
Reference: AM 117626

To appear in: *Acta Materialia*

Received date: 21 June 2021
Revised date: 30 November 2021
Accepted date: 4 January 2022

Please cite this article as: Daniel Wicht, Alexander Kauffmann, Matti Schneider, Martin Heilmaier, Thomas Böhlke, On the impact of the mesostructure on the creep response of cellular NiAl-Mo eutectics, *Acta Materialia* (2022), doi: https://doi.org/10.1016/j.actamat.2022.117626

Graphical Abstract

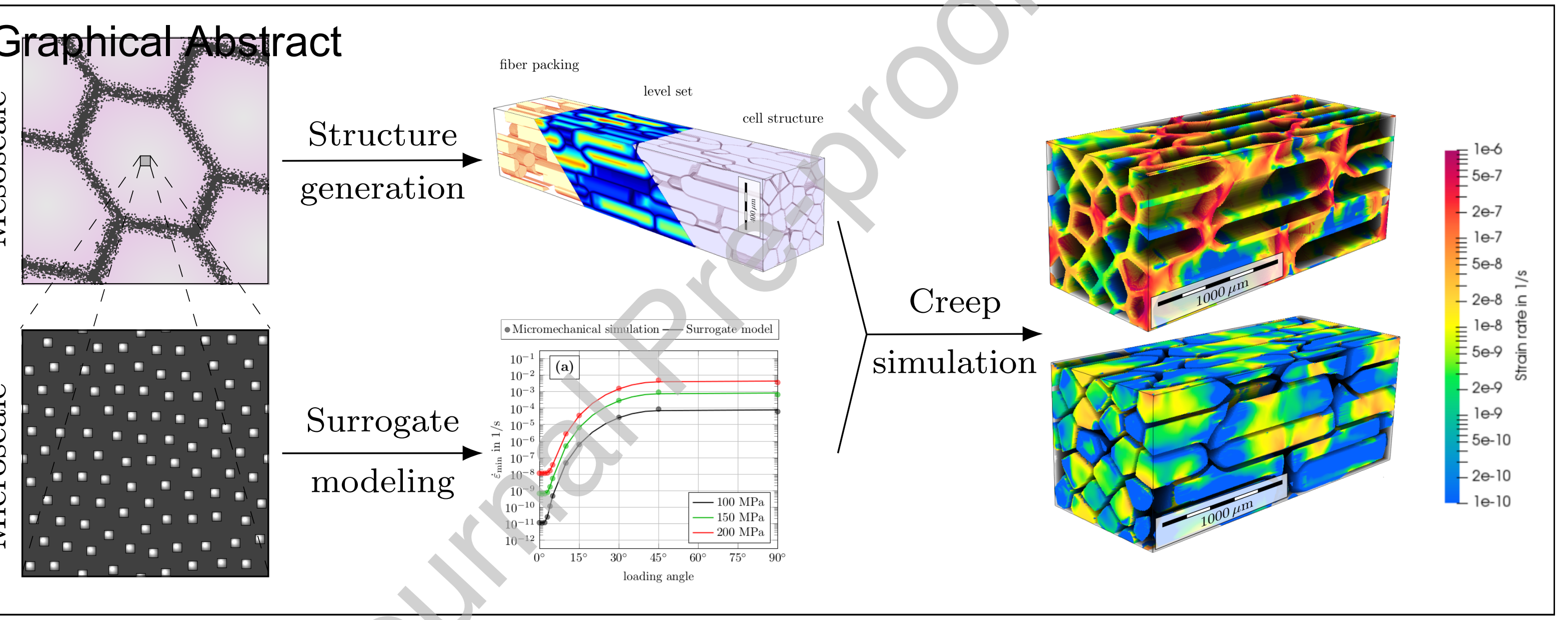

On the impact of the mesostructure on the creep response of cellular NiAl-Mo eutectics

Daniel Wicht[a], Alexander Kauffmann[b], Matti Schneider[a], Martin Heilmaier[b], and Thomas Böhlke[a,*]

[a]Institute of Engineering Mechanics, Karlsruhe Institute of Technology (KIT), Kaiserstraße 10, 76131 Karlsruhe, Germany; `{daniel.wicht, matti.schneider, thomas.boehlke}@kit.edu`
[b]Institute for Applied Materials, Karlsruhe Institute of Technology (KIT), Engelbert-Arnold-Straße 4, 76131 Karlsruhe, Germany; `{alexander.kauffmann, martin.heilmaier}@kit.edu`
*Correspondence to `thomas.boehlke@kit.edu`

January 18, 2022

Abstract

Abstract
Directionally solidified eutectics of NiAl matrix and fibrous refractory metals, like Mo, can form cellular mesostructures with significant fiber misalignment and changing fiber volume fraction, for example, when being solidified at high growth rates or when increased solidification intervals are present in the alloys. In order to reveal the deteriorating impact of the mesostructure, i.e., the volume fraction and aspect ratio of the well-aligned cells, on the creep response of such cellular eutectics, we rely on scale-bridging numerical simulations, using the level-set framework by Sonon et al. [1] for microstructure generation and FFT-based solvers for computing the creep response. Our results indicate, firstly, that the fraction of properly aligned regions in cellular NiAl composites is lower than estimated in earlier experimental studies, due to the existence of degenerated regions surrounding the well-aligned cell interiors. Secondly, studying the influence of the cell aspect ratio shows that the apparent stress exponent of the composite is very sensitive with respect to this parameter, providing a possible explanation for the large scatter of experimentally determined stress exponents in previous studies. A comparison of the numerical simulations to a linear rule of mixtures and the frequently applied analytical Kelly-Street model illustrates that both fail to accurately describe the magnitude of minimum creep rates in the investigated ranges of volume fractions and aspect ratios. The heterogeneity of the strain-rate field on the mesoscale is identified as the primary error source, demonstrating that either numerical simulations or more sophisticated analytical models are required for reliably predicting for the creep response of cellular materials.

Keywords: Directional solidification, Nickel-aluminides, Creep, Micromechanical modeling, Level-set methods

1 Introduction

Alloys based on the intermetallic compound NiAl feature a number of attractive properties, such as high solidus temperatures, low density and excellent oxidation resistance [2], making them appealing candidates for novel structural high-temperature materials. However, binary NiAl lacks sufficient creep resistance at high temperatures. As a result, research effort was devoted to improving the creep behavior by introducing body-centered cubic refractory metals such as Mo or Cr to the B2-ordered NiAl, forming in-situ eutectic two-phase microstructures. Bei and George [3] used directional solidification to produce microstructures consisting of well-aligned single-crystalline Mo fibers embedded in an NiAl matrix. It was found that the Mo-fibers were virtually dislocation free [4, 5], resulting in a high yield strength [6] and an increase in creep resistance by several orders of magnitude in strain-rate for a given applied stress [7–9]. Motivated by these experimental findings, Albiez et al. [10] proposed suitable single-crystal material models for the NiAl-matrix and the Mo-fibers and studied the creep behavior of the well-aligned composite through crystal plasticity simulations. In a subsequent study [11], the models were extended by a non-local gradient-plasticity approach to account for the movement and transfer of dislocations. Overall, both experimental studies and simulations significantly improved the understanding of the creep behavior of well-aligned NiAl-Mo composites.

However, several studies [7,12,13] demonstrated that the microstructure of directionally solidified NiAl-Mo is rather sensitive to the manufacturing process. In particular, insufficient temperature gradients and/or high growth rates, which are desirable from the viewpoint of industrial application, lead to deviations from an ideal microstructure of perfectly aligned fibers in the NiAl matrix. NiAl-Mo develops cellular structures [12, 13] in which regions of well-aligned fibers are surrounded by degenerated regions with higher NiAl fraction and coarse, misaligned Mo fibers, see Fig. 1. Indeed, Gombola et al. [14] revealed that similar structures emerge for various compositions in the NiAl-(Mo,Cr) system.

Seemüller et al. [13] showed that cell formation results in a lower creep resistance, between well-aligned NiAl-Mo and binary NiAl. The ability to model and predict the creep behavior of cellular NiAl based composites appears crucial, as: (i) Perfect laboratory conditions for producing NiAl-based eutectics may not always be available in an industrial context where high growth rates are preferred. (ii) The process conditions to achieve perfect alignment become challenging in case of advanced complex alloying compositions with extended solidification intervals [14]. The applied temperature gradients need to cover the solidification interval in the transition zone from the liquid to the solids in order to obtain stable processing conditions during solidification. Thus, cellular microstructures become more likely under practical conditions. Determining the impact of partially interrelating morphological features, such as cell volume fraction and aspect ratio, on the mechanical behavior is necessary, not only to assess the sensitivity of the overall creep response to microstructural irregularities, but also for identifying suitable processing conditions and alloy compositions. Finally, a rather large disparity on reported experimental results, for example regarding the apparent stress exponent of the composite [8–10, 13], might indicate that the mesostructure of the material has already played a role in some of the previous studies as will be highlighted in Sec. 2.2 and Sec. 4.4.

Thus, the aim of the present study is to investigate the creep behavior of cellular NiAl-Mo through creep simulations on the microscale. To this end, we use modern FFT-based methods [15], which have established themselves as powerful algorithms for computing the effective response of microstructured materials, such as composites [16, 17] and polycrystals [18, 19]. In the context of micromechanical creep simulations, the effective strain-rate is computed by volume averaging the strain-rate field on the microstructure level, which arises in response to a prescribed mean stress. The main difficulty for this task lies in the multi-scale nature of the problem, i.e., the difference in the characteristic length scales of the different geometric features of the material, see Fig. 1. While the cellular colonies are roughly 1 mm and 0.2 mm in length and diameter, respectively, the diameter of the Mo fibers is in the sub-micron scale. Hence, if a volume element with multiple cells is considered for simulating the creep behavior, resolving the individual fibers will be infeasible. Instead, we follow Seemüller et al. [13] and divide the material on the mesoscale into soft regions for the boundary, behaving similar to the NiAl-matrix, and homogeneous hard regions, mirroring the effective creep behavior of the well-aligned NiAl-Mo colonies.

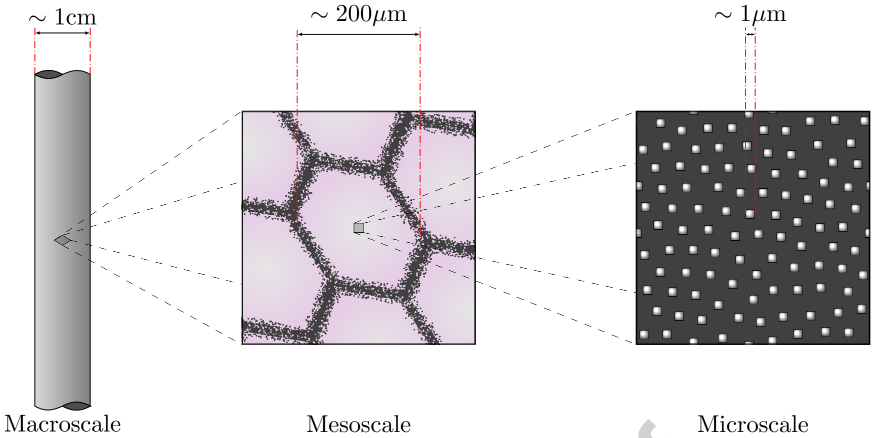

Figure 1: Structure of directionally solidified cellular NiAl-Mo sketched at different length scales based on dark field optical microscopy images by Seemüller et al. [13]

In order to bridge the different length scales involved in the simulations, we proceed with the following steps:

1. A phenomenological surrogate model for the anisotropic creep response of the single well-aligned colonies is calibrated based on crystal plasticity simulations following Albiez et al. [10] in Sec. 2.
2. Synthetic microstructures, mirroring the geometrical features of cellular NiAl-Mo, are generated based on the level set framework of Sonon et al. [1, 20, 21], see Sec. 3.
3. Having gathered all necessary prerequisites, the effective creep behavior of cellular NiAl-Mo is investigated through FFT-based micromechanics simulations in Sec. 4.

2 Modeling the anisotropic creep behavior of well-aligned NiAl-Mo colonies

2.1 Single crystal plasticity model for fiber and matrix

In the following, we briefly review the material models and parameters [10] used for characterizing the anisotropic creep response of well-aligned NiAl-Mo. The material behavior of the NiAl-matrix and the Mo-fibers is governed by a classical small-strain single-crystal elasto-viscoplasticity model. In the following, ε denotes the infinitesimal strain tensor and σ refers to the Cauchy stress tensor. Tensor contractions are marked by dots, i.e, a single tensor contraction is denoted by $\cdot$ and a double tensor contraction reads $:$. For instance, with vectors u, v, second order tensors A, B, and a forth order tensor $\mathbb{C}$, the expressions $u = A \cdot v$ and $A = \mathbb{C} : B$ are equivalent to $u_i = A_{ij} v_j$ and $A_{ij} = C_{ijkl} B_{kl}$, respectively, in index notation using the summation convention. The linear elastic material behavior is governed by Hooke's law for the elastic strains ε_e

$$\sigma = \mathbb{C} : (\varepsilon - \varepsilon_\mathrm{p}) \quad \text{with} \quad \varepsilon = \varepsilon_\mathrm{e} + \varepsilon_\mathrm{p} \tag{2.1}$$

and the stiffness tensor $\mathbb{C}$. The plastic strain ε_p due to dislocation glide is realized as a linear combination of simple shears [22] in crystallographic slip systems characterized by their slip direction d_α and slip plane normal n_α, where the subindex $(\cdot)_\alpha$ refers to the αth of N slip systems. Assuming that the slip in the glide systems follows the classical power-law flow rule of Hutchinson [23], the flow rule reads

$$\dot{\varepsilon}_{\mathrm{p}} = \sum_{\alpha=1}^{N} \dot{\gamma}_0 \, \mathrm{sgn}(\tau_\alpha) \left| \frac{\tau_\alpha}{\tau^{\mathrm{F}}} \right|^m d_\alpha \otimes^s n_\alpha, \tag{2.2}$$

with shear stress $\tau_\alpha = \sigma : (d_\alpha \otimes^s n_\alpha)$, yield stress τ^{F}, reference slip rate $\dot{\gamma}_0$ and stress exponent m. We emphasize that the chosen flow rule only covers plasticity due to conservative dislocation glide. More sophisticated models which include the smaller strain contribution of dislocation climb by adding additional non-conservative modes of deformation have been proposed, for instance, by Lebensohn et al. [24]. However, as Albiez et al. [10] demonstrate, the chosen approach (2.2) is able to predict the creep behavior of NiAl-Mo for temperatures between 900°C and 1000°C and stresses between 100 MPa and 250 MPa with good accuracy. Furthermore, the stress exponents m of the monolithic phases as well as of the composite are significantly larger than 1 indicating that diffusional contributions to the overall strain are negligible. Hence, to avoid the introduction and calibration of additional unknown material parameters, we restrict to the glide based formulation. Furthermore, the temperature dependence of the creep behavior is incorporated in the reference shear rate by Albiez et al. [10], using an Arrhenius approach. As an exemplifying study, we compare our modeling results mainly with the experiments by Seemüller et al. [13], who carried out creep tests at 900°C. All material parameters, experimental data and simulation results in the this study are given for this fixed temperature. In addition, experimental results show that the softening of the Mo-fibers, i.e., the decrease of τ^{F} during creep, is only weakly pronounced in the cellular material, see Fig. 5 in Seemüller et al. [13]. Computational investigations suggest that, even for the well-aligned material, substantial softening only occurs for direct loading in fiber direction, see Wicht et al. [25, Sec. 6.3.3]. For a thorough investigation of this load case and a physical interpretation of the softening, we refer to the studies of Albiez et al. [10, 11]. As the present study focuses on cellular NiAl-Mo, we restrict to investigating the steady-state creep rate of the materials, i.e., we treat τ^{F} as constant.

NiAl	$C_{11} = 184\,\mathrm{GPa}$	$C_{12} = 121\,\mathrm{GPa}$	$C_{44} = 88.1\,\mathrm{GPa}$
	$\tau^{\mathrm{F}} = 30.75\,\mathrm{MPa}$	$\dot{\gamma}_0 = 8.45 \times 10^{-6}\,\mathrm{s}^{-1}$	$m = 5.8$
Mo-Fibers	$C_{11} = 410\,\mathrm{GPa}$	$C_{12} = 163\,\mathrm{GPa}$	$C_{44} = 100\,\mathrm{GPa}$
	$\tau^{\mathrm{F}} = 3751\,\mathrm{MPa}$	$\dot{\gamma}_0 = 3.43 \times 10^{-1}\,\mathrm{s}^{-1}$	$m = 10$

Table 1: Material parameters for NiAl and Mo at 900°C [10, 13]

The material parameters for NiAl and the Mo-fibers are mostly taken from Albiez et al. [10], see Tab. 1. By comparing the yield strength τ^{F} of the two materials at 900°C, the difference in creep resistance becomes apparent. Due to the directional solidification process, the Mo-fibers are virtually free of dislocations [4,5], leading to a high yield strength of roughly 3% of the shear modulus of Mo. Based on an extensive literature review, Albiez et al. [10] were able to adopt most material parameters from existing sources. Indeed, among the relevant parameters for the present study, only the reference shear rate of the Mo-fibers was calibrated to match simulation results [10]. However, as the study of Seemüller et al. [13] represents our primary point of comparison, we adopt two additional changes with respect to the parameters of NiAl. More precisely, we choose $m = 5.8$ as measured by Seemüller et al. [13], compared to 4.04 used by Albiez et al. [10]. Indeed, a large range of values from 3 to 7 has been reported for the stress exponent of single-phase NiAl in the literature [2]. The large scatter in experimental measurements may be due to the sensitivity of the stress exponent of near stoichiometric NiAl on composition, as noted by Whittenberger [26]. To compensate for the change in the stress exponent, the value of $\dot{\gamma}_0$ was modified to reach a decent agreement between modeled material behavior and experimental measurements, see Fig. 2(c).

2.2 Minimum creep rate of well-aligned NiAl-Mo under various loading angles

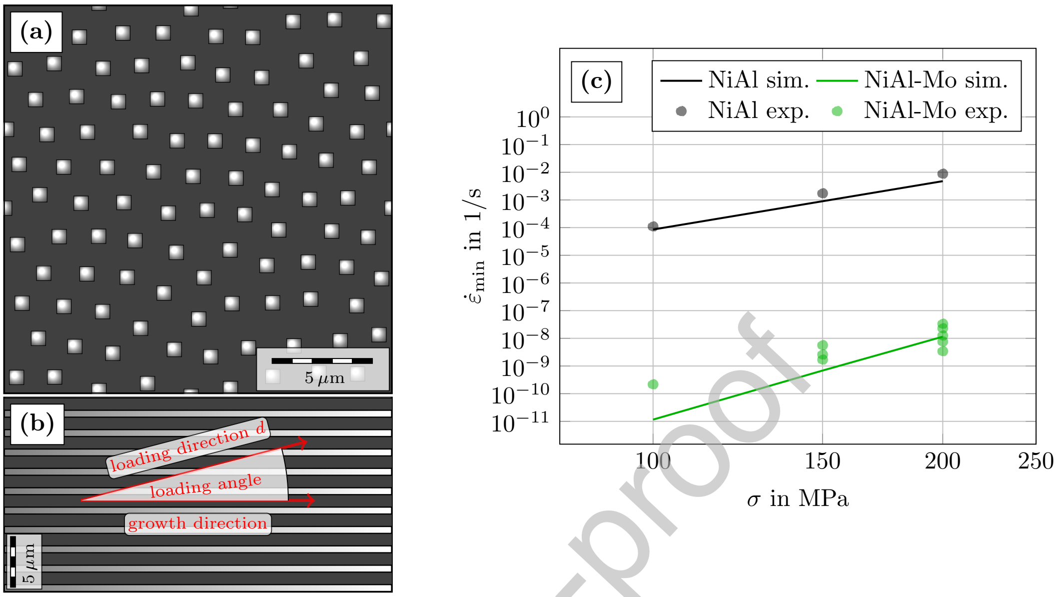

Figure 2: (a) Transverse section of the two-dimensional well-aligned NiAl-Mo microstructure used in FFT-computations; (b) Sketch of a longitudal section of well-aligned NiAl-Mo indicating growth direction and loading angle; (c) Comparison of micromechanical simulations and experimental results by Seemüller et al. [13] for binary NiAl and well-aligned NiAl-Mo

For characterizing the material behavior of well-aligned NiAl-Mo, we use the two-dimensional cell shown in Fig. 2(a), with 100 fibers occupying 14% of the total area [3]. Distinct microstructural features of well-aligned NiAl-Mo include the square cross-section of the Mo-fibers and their regular arrangement in a hexagonal pattern, see Bei and George [3, Fig. 1] or Seemüller et al. [13, Fig. 3]. To generate a similar hexagonal arrangement, we use the mechanical contraction algorithm of Williams and Philipse [27] to generate a circle packing with 70% volume fraction. Subsequently, square fibers of appropriate size are placed at the centers of the packed circles. The resulting structure is discretized by 256 × 256 pixels. For investigating the anisotropic creep behavior of the material, we apply periodic boundary conditions and prescribe the effective stress tensor $\bar{\sigma}$, i.e., the volume average of the stress field. More precisely, the prescribed effective stress tensor has the form $\bar{\sigma} = \sigma\, d \otimes d$ corresponding to a uniaxial stress state with magnitude σ and loading direction d. The loading is applied in 1 s and held until a steady-state strain-rate is reached. Different loading directions n are tested with respect to their angle of misalignment to the growth direction, see Fig. 2(b) for a sketch. Details on the computational setup of the FFT-based micromechanics solver are given in Sec. 4.1. The computed minimum creep rate of the well-aligned material for loadings in growth direction at various stress levels is compared to the creep experiments by Seemüller et al. in Fig. 2(c). Although the data from simulation and experiment are in decent agreement in the range from 150 – 200 MPa, the slopes, i.e., the apparent stress exponents, differ notably, with $m = 10$ in the simulations compared to values of 5 to 7 in Seemüller et al. [13]. This indicates that the Mo-fibers control the creep behavior of the single colony in the simulation. A broader review of existing creep studies reveals that there is, in fact, no clear consensus on the stress exponent of well-aligned NiAl-Mo. For instance, creep experiments by Haenschke et al. [7], Albiez et al. [10] and Dudová et al. [8] displayed fiber-dominant behavior with m between 10 and 14. In contrast, Seemüller et al. [13] and Hu et al. [9] measure an exponent in the range of $4-7$. Taking a closer look at the anisotropic creep behavior predicted by the microstructure computations, see Fig. 3, elucidates the disparity in experimental measurements. Fig. 3(a) reveals the pronounced sensitivity of the creep behavior with respect to the angle of misalignment between loading and fiber direction. For loading angles larger than 5°, the creep rate quickly increases by orders of magnitudes. Indeed, between 15° and 30°, the reinforcing effect of the fibers mostly vanishes and the creep rate approaches that of the pure NiAl matrix. A more subtle change in behavior can be observed at small angles of misalignment, see Fig. 3(b). Between 0° to 2°, we observe no change in creep behavior and the apparent stress exponent corresponds to that of the Mo-fibers. However, between 3° to 4°, there is a turning point from fiber-controlled to matrix-controlled creep, with little change in the overall magnitudes of creep rates (at least between $150-200\,\mathrm{MPa}$). This offers a possible explanation for the wide range of determined stress exponents in the aforementioned experimental studies, as a small misalignment with respect to the loading direction has a notable impact on the measured rates. In Sec. 4.3, we identify the mesostructure of the material as another plausible source for the scatter in stress exponents.

Overall, we conclude that the material model and parameters by Albiez et al. [10] lead to a good agreement of micromechanical simulations with experimental results, in particular when taking the sensitivity of the material behavior with respect to load angle into account. Indeed, the creep data by Seemüller et al. [13] matches the computational results for a loading angle of 4° almost perfectly, see Fig. 2(c) and Fig. 3(b). Having validated the model and computations on the microscale, we use the obtained results to calibrate a surrogate model, mimicking the effective behavior of the well-aligned fibrous material.

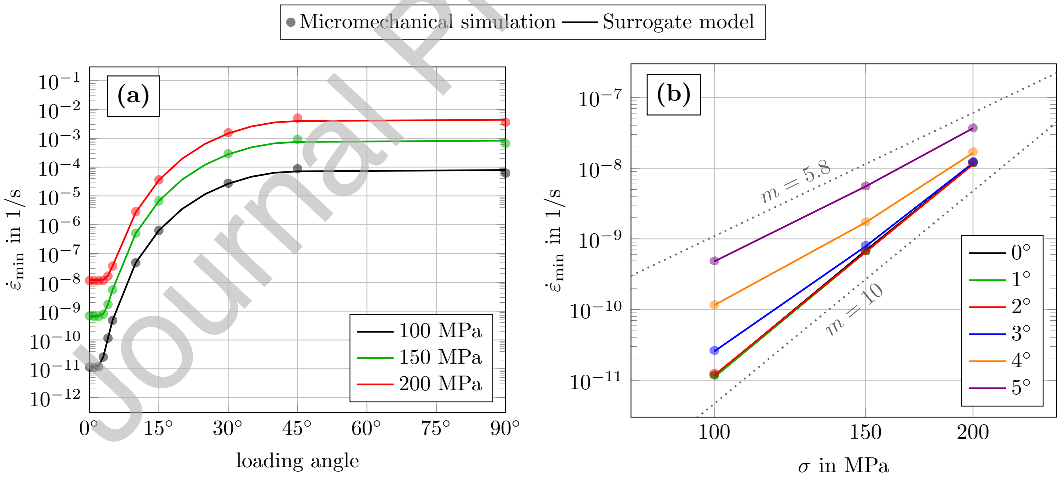

Figure 3: Comparison of FFT-based simulations on well-aligned NiAl-Mo microstructures and the surrogate model (2.8) for uniaxial creep tests where the loading angle is given with respect to growth direction: (a) Minimum creep rate vs loading angle; (b) Norton plot for small loading angles

2.3 Phenomenological model for the well-aligned fiber structure

The objective of the section at hand is to develop a simple phenomenological elasto-viscoplastic material model which is able to capture the creep behavior observed in Sec. 2.2. In particular, the following properties should be reflected by the model:

1. The transverse isotropy of both stiffness and flow rule, induced by the microstructure.
2. The directional dependence of the apparent stress exponent, resulting from the difference in fiber and matrix behavior.

The effective linear elastic behavior is governed by Hooke's law (2.1), where the components of the effective stiffness tensor are readily obtained by six linear elastic computations. The computed stiffness tensor is almost transversely isotropic, with a relative error below 0.1%. The associated engineering constants are listed in Tab. 2. For the flow rule, we rely on the transversely isotropic splitting of the deviatoric stress tensor by Naumenko-Altenbach [28]

$$\sigma' = \sigma'_{\mathrm{L}} + \sigma'_{\mathrm{P}} + \sigma'_{\mathrm{S}} \tag{2.3}$$

into a longitudinal component σ'_{L}, the plane stress σ'_{P} and the remaining out-of-plane shear stress σ'_{S}, defined by

$$\sigma'_{\mathrm{L}} = \left(\frac{3}{2}\sigma : (n \otimes n) - \operatorname{tr}(\sigma)\right)\left(n \otimes n - \frac{1}{3}\,\mathrm{Id}\right), \tag{2.4}$$

$$\sigma'_{\mathrm{P}} = (\mathrm{Id} - n \otimes n) \cdot \sigma \cdot (\mathrm{Id} - n \otimes n) - \frac{1}{2}(\operatorname{tr}(\sigma) - \sigma : (n \otimes n))(\mathrm{Id} - n \otimes n), \tag{2.5}$$

$$\sigma'_{\mathrm{S}} = 2(n \cdot \sigma \cdot (\mathrm{Id} - n \otimes n)) \otimes^{s} n, \tag{2.6}$$

respectively. Here, n denotes the unit normal of the isotropic plane, i.e., the fiber direction. Naumenko-Altenbach [28] show that the Frobenius norms $\|\sigma'_L\|$, $\|\sigma'_P\|$ and $\|\sigma'_S\|$ of the stress components constitute a set of independent, transversely isotropic invariants of σ'. Thus, for any flow potential of the form $\Phi(\sigma') = \widehat{\Phi}(\|\sigma'_L\|, \|\sigma'_P\|, \|\sigma'_S\|)$, the associated flow rule $\dot{\varepsilon}_{\mathrm{P}} = \frac{\partial \Phi}{\partial \sigma'}(\sigma')$ is transversely isotropic. For the present model, we use the simple ansatz

$$\Phi(\sigma') = \dot{\varepsilon}_0 \left(\frac{\sigma_{\mathrm{L}}^{\mathrm{F}}}{m_{\mathrm{L}}+1} \left| \frac{\|\sigma'_{\mathrm{L}}\|}{\sigma_{\mathrm{L}}^{\mathrm{F}}} \right|^{m_{\mathrm{L}}+1} + \frac{\sigma_{\mathrm{P}}^{\mathrm{F}}}{m_{\mathrm{P}}+1} \left| \frac{\|\sigma'_{\mathrm{P}}\|}{\sigma_{\mathrm{P}}^{\mathrm{F}}} \right|^{m_{\mathrm{P}}+1} + \frac{\sigma_{\mathrm{S}}^{\mathrm{F}}}{m_{\mathrm{S}}+1} \left| \frac{\|\sigma'_{\mathrm{S}}\|}{\sigma_{\mathrm{S}}^{\mathrm{F}}} \right|^{m_{\mathrm{S}}+1} \right), \tag{2.7}$$

which leads to the flow rule

$$\dot{\varepsilon}_{\mathrm{P}}(\sigma') = \dot{\varepsilon}_0 \left(\left| \frac{\|\sigma'_{\mathrm{L}}\|}{\sigma_{\mathrm{L}}^{\mathrm{F}}} \right|^{m_{\mathrm{L}}} \frac{\sigma'_L}{\|\sigma'_{\mathrm{L}}\|} + \left| \frac{\|\sigma'_{\mathrm{P}}\|}{\sigma_{\mathrm{P}}^{\mathrm{F}}} \right|^{m_{\mathrm{P}}} \frac{\sigma'_P}{\|\sigma'_{\mathrm{P}}\|} + \left| \frac{\|\sigma'_{\mathrm{S}}\|}{\sigma_{\mathrm{S}}^{\mathrm{F}}} \right|^{m_{\mathrm{S}}} \frac{\sigma'_S}{\|\sigma'_{\mathrm{S}}\|} \right), \tag{2.8}$$

i.e., each stress component σ'_{L}, σ'_{P}, σ'_{S} has an associated yield stress $\sigma_{\mathrm{L}}^{\mathrm{F}}$, $\sigma_{\mathrm{P}}^{\mathrm{F}}$, $\sigma_{\mathrm{S}}^{\mathrm{F}}$ and the stress exponent m_{L}, m_{P}, m_{S}, respectively. In contrast to the equivalent-stress approach by Naumenko-Altenbach [28], the present formulation is able to accommodate different stress exponents for longitudinal and in-plane loadings. On the downside, our flow rule does not reduce to the classical J_2-plasticity model for a specific choice of parameters.

The material parameters for the flow rule, see Tab. 2, were calibrated by performing a creep test in fiber direction and two shear-creep tests. The resulting creep behavior of the surrogate model is compared to the crystal plasticity computations of Sec. 2.2 in Fig. 3. Overall, the surrogate model matches the simulations exceptionally well. Both, the deterioration of creep resistance for off angle loadings, see Fig. 3(a), and the transition from fiber to matrix-dominated creep at small angles, see Fig. 3(b), are reproduced with high accuracy. Overall, the surrogate model is suitable for facilitating computational investigations on cellular NiAl-Mo on the mesoscale. However, some remarks on the limitations of the model are in order:

1. The largest relative error in strain-rates between surrogate model and micromechanical crystal plasticity simulation is around 25% for loadings perpendicular to the fibers. This is acceptable for investigations of the creep behavior, where creep rates are typically visualized on a logarithmic scale and experimentally determined creep rates may scatter up to an order of magnitude. However in other contexts, e.g., for predicting the non-linear stress-strain behavior, the model may have to be reviewed, or, at least, carefully recalibrated.

2. Both simulations [10,11] and experiments [8,9,13] on well-aligned NiAl-Mo show a transient decrease of the creep rate in the initial stages of a creep test, owing to the load transfer from fibers to matrix. Naturally, the surrogate model cannot account for this behavior as the constituent phases are not explicitly resolved.

Stiffness	$E_\mathrm{L} = 120.6\,\mathrm{GPa}$	$E_\mathrm{T} = 181.9\,\mathrm{GPa}$	$G_\mathrm{LT} = 89.7\,\mathrm{GPa}$	$\nu_\mathrm{TT} = 0.015$	$\nu_\mathrm{LT} = 0.379$
Creep	$\sigma_\mathrm{L}^\mathrm{F} = 625\,\mathrm{MPa}$	$\sigma_\mathrm{P}^\mathrm{F} = 153.5\,\mathrm{MPa}$	$\sigma_\mathrm{S}^\mathrm{F} = 154.5\,\mathrm{MPa}$	$\dot{\varepsilon}_0 = 0.01\,\mathrm{s}^{-1}$	
	$m_\mathrm{L} = 10$	$m_\mathrm{P} = 5.8$	$m_\mathrm{S} = 5.8$		

Table 2: Material parameters for the surrogate model, mimicking the creep behavior of unidirectional NiAl-Mo with 14% fiber fraction

3 Generation of synthetic cellular mesostructures

For NiAl-10Mo alloys solidified at a rate of 80 mm/h, Seemüller et al. [13] observed that regions of well-aligned unidirectional fibers formed cellular structures on the meso-scale, surrounded by misaligned fibers and pure matrix material. The cells, featuring roughly hexagonal cross-sections, were elongated in the direction of solidification, with lengths of around $1000\,\mu$m and an aspect ratio of five. Based on a cell distance between $6 - 10\,\mu$m, Seemüller et al. [13] estimated a volume fraction of $82 - 85\%$ of the hard regions.

For generating synthetic volume elements, mimicking the aforementioned characteristics, we rely on the level-set-based framework of Sonon et al. [1, 20, 21]. In the following, the basic methodology is briefly summarized for the convenience of the reader. Suppose we have a rectangular cell Y in $\mathbb{R}^d$ with a set of non-overlapping particles $\Phi = \bigcup_{i=1}^N \Phi_i$. Sonon et al. propose an implicit description of the microstructure in terms of the nearest neighbour level set

$$DN_1(x) = \begin{cases} \min\limits_{y \in \partial\Phi} d(x,y), & x \notin \Phi, \\ \min\limits_{y \in \partial\Phi} -d(x,y), & x \in \Phi, \end{cases}$$

where $d(x,y)$ denotes the periodic distance of two points $x, y \in Y$ and $\partial\Phi$ stands for the boundary of the set Φ. Thus, the condition $DN_1(x) \leq 0$ describes the space occupied by particles. As an extension to $DN_1(x)$, the level sets $DN_k(x)$ may be computed [1], encoding the periodic distance at each point to the k-th nearest particle Φ_i. The $DN_k(x)$ level sets may be used in the context of dense packing algorithms and/or for generating new microstructures by thresholding suitable level-set functions [1, 20, 21]

$$f(DN_1(x), DN_2(x), \ldots, DN_{k_\mathrm{max}}(x)) \leq 0.$$

In particular, for the present study, we exploit the Voronoi-type level set with interparticle distance t

$$DN_1(x) - DN_2(x) + t \leq 0, \tag{3.1}$$

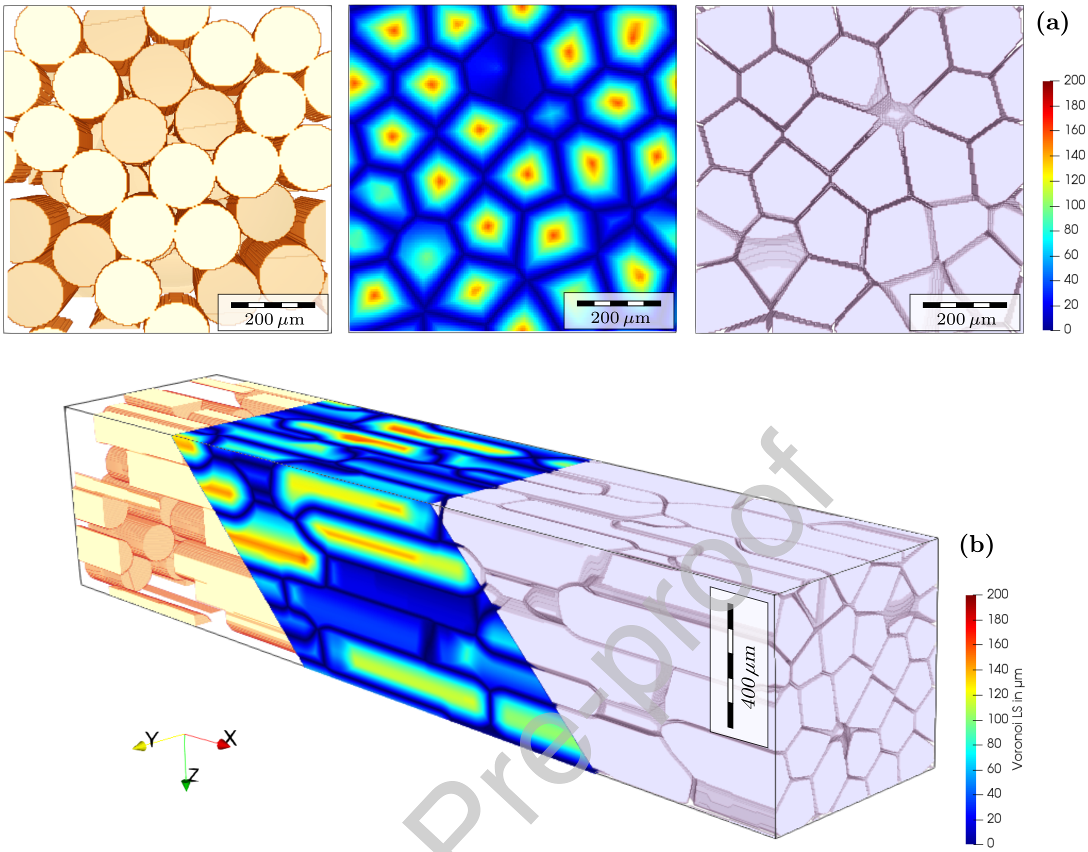

Figure 4: Different stages of the microstructure generation process for (a) a transverse cross section and (b) a 3D overview with the underlying fiber structure (left), the Voronoi level set (3.1) of the center lines (middle) and the final cell structure (right)

for generating microstructures with the complex geometrical features of cellular NiAl-Mo. For a given collection of particles, $DN_1(x) - DN_2(x) = 0$ describes the boundary of the associated Voronoi tessellation. Thus, the geometry extracted by the related level set (3.1) may be interpreted as an expansion of all particles to a shape which enforces a uniform distance of t between the resulting cells, see Sonon et al. [1, Sec. 4.1]. In two dimensions, Massart et al. [29] used the level set (3.1) to generate irregular masonry structures featuring elongated inclusions, resembling the cells observed in NiAl-10Mo. We follow a similar approach to generate the microstructures for the present study:

1. For given cell dimensions, we use the sequential addition and migration (SAM) algorithm [30] to pack cylindrical fibers with a length of 800 μm and a diameter of 160μm until a volume fraction of at least 45% is reached. The SAM method has proven to be a flexible and powerful scheme for generating dense packings of non-overlapping short-fibers with arbitrary prescribed orientation state and thus represents our algorithm of choice. However, for the simple uni-directional case, the method may be substituted by any algorithm which is capable of reaching the desired volume fraction. For instance, the LS-RSA method by Sonon et al. [1] may be adapted for elongated inclusions to integrate the level-set computation in the packing algorithm. As the level-set operation (3.1) further enlarges the inclusions, the fiber dimensions were chosen 20% smaller than those observed for the cells in

the alloy. The volume fraction was chosen to obtain a dense fiber packing, i.e., a roughly hexagonal pattern, which still permits some irregularity as observed in the actual microstructure.

2. The level sets $DN_1(x)$ and $DN_2(x)$ are computed based on the center lines of the fibers. For efficiently computing the level sets, we rely on the Euclidean distance transform by Meijster et al. [31], see Appendix A for further details.

3. Using the bisection method, we iteratively solve for the cell distance t until a prescribed cell volume fraction ϕ is obtained. With the indicator function

   $$i_V(x) = \begin{cases} 1, & DN_1(x) - DN_2(x) + t \leq 0, \\ 0, & \text{otherwise}, \end{cases}$$

   of the level set (3.1), we terminate when the convergence criterion

   $$\left| \frac{\int_Y i_V(x) \mathrm{d}V}{\int_Y \mathrm{d}V} - \phi \right| < \delta$$

   is satisfied. Throughout we set the tolerance for the volume fraction to $\delta = 10^{-3}$. Unless stated otherwise, the prescribed volume fraction is set to $\phi = 85\%$, following the estimate of Seemüller et al. [13]. Note that we prefer to fix the volume fraction ϕ rather than the interparticle distance t, as, from the viewpoint of micromechanics, the volume fraction enters the effective (linear elastic) material behavior to first order [32, Ch. 14].

Note that, in practice, the discrete level set is computed on a regular background grid. Throughout the present study, we choose the same refinement for the level-set computation as for the target resolution of the microstructure used in the FFT-based computations. More precisely, for a given underlying fiber packing, steps 2 and 3 of the outlined process are repeated for each realized resolution. Compared to downsampling all realizations from a single finely resolved microstructure, this approach requires a larger number of level-set computations. However, it offers tighter control of the target volume fraction, which is preferred with respect to the minimum necessary resolution for the FFT-based computations, see Sec. 4.2. The processing steps for a generated microstructure with dimensions $4000\,\mu\text{m} \times 800\,\mu\text{m} \times 800\,\mu\text{m}$ are visualized in Fig. 4. Due to the dense fiber packing, the placement and aspect ratio of the cells closely follow that of the underlying fibers. Note that smaller fragments visible in Fig. 4 arise as artifacts of the 2D cuts and are actually part of regularly sized cells. A transverse section and a longitudinal section of the generated structure are compared to dark field optical microscopy images of cellular samples by Seemüller et al. [13] in Fig. 5. Both the roughly hexagonal cross section of the cells and their elongated shape with an aspect ratio about five are featured in the synthetic structure. Hence, the volume elements generated by the adapted level-set strategy closely resemble cellular NiAl-Mo, enabling subsequent micromechanical studies on the materials' effective creep behavior.

4 Creep behavior of cellular multi-colony NiAl-Mo eutectics with degenerated boundary regions

4.1 Computational setup

For computing the effective creep response of the NiAl-Mo alloys, we rely on an in-house FFT-based micromechanics solver, written in Python 3.7 with Cython extensions and parallelized using OpenMP.

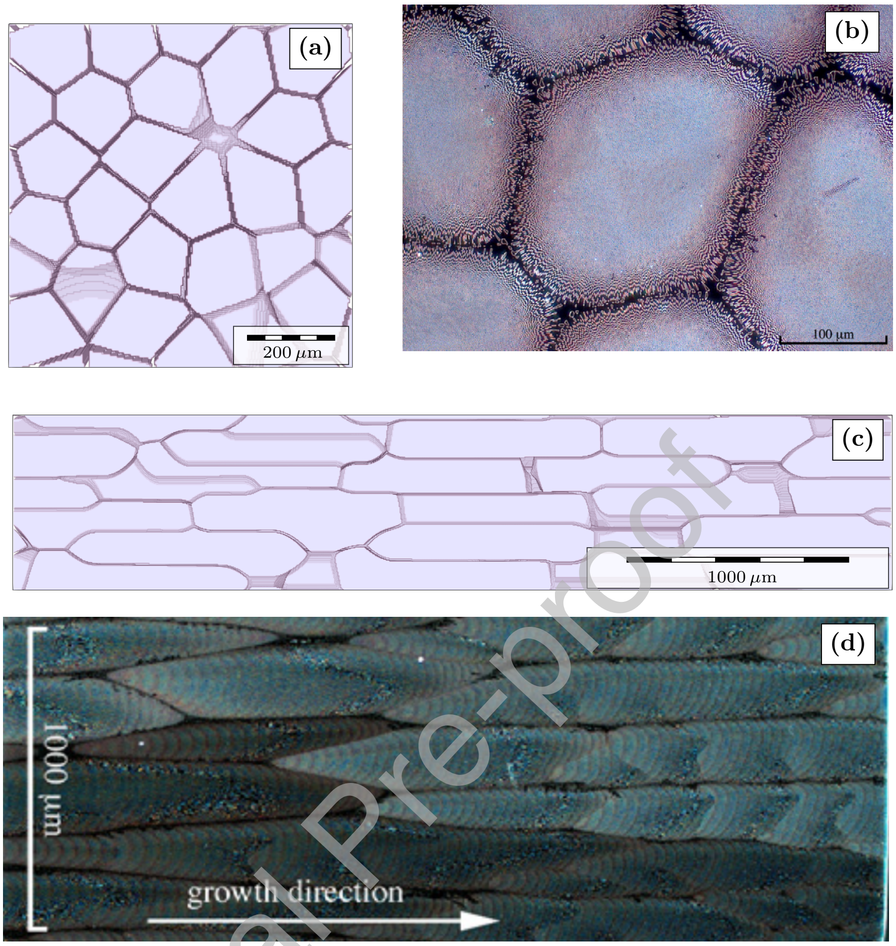

Figure 5: Synthetic generated microstructures in comparison to dark field optical microscopy images of NiAl-Mo by Seemüller et al. [13]: (a)-(b) Comparison of transverse cross sections; (c)-(d) Comparison of longitudal cross sections[1]

More precisely, we use the BFGS-CG algorithm [33] in combination with the staggered grid discretization [34]. We refer to the recent review by Schneider [35] for a general overview of current FFT-based methods and the articles by Segurado et al. [36] and Lebensohn-Rollett [37] for dedicated reviews on the computational homogenization of polycrystalline materials. For a detailed discussion of the specific algorithms used in the study at hand, see Wicht et al. [33]. FFT-based solvers naturally operate with periodic boundary conditions, i.e., the stress and strain fields in the volume element are periodic. For our investigations, we prescribe an effective stress $\bar{\sigma}$, which is the volume average of the stress field, of the form $\bar{\sigma} = \sigma\, d \otimes d$, corresponding to a uniaxial stress state with magnitude σ in direction d, see Kabel et al. [38]. The loading is applied in 1 s and subsequently held constant until a steady-state creep rate is reached. For our investigation of the cellular material, we restrict to loadings in growth direction.
Throughout, convergence of the FFT-based solver is checked using the criterion proposed in Sec. 5 by Schneider et al. [39] with a prescribed tolerance of 10^{-4}. For the soft regions in the cell-boundary regions,

---

[1] Fig. 5(b) and Fig. 5(d) from Seemüller et al. [13] are reused under the STM permissions guidelines: `https://www.stm-assoc.org/intellectual-property/permissions/permissions-guidelines/`.

we use the material model of NiAl, see Sec. 2.1. The behavior of the hard regions in the well-aligned cells is governed by the surrogate model proposed in Sec. 2.3. All computations were either performed on a workstation with two 12-core Intel Xeon(R) Gold 6146 CPUs and 512 GB RAM or a workstation with two AMD EPYC 7642 with 48 cores each and 1024 GB RAM.

4.2 Study on the size of the representative volume element

FFT-based micromechanics solvers naturally operate on a regular (voxel)grid. However, even when treating the hard regions in cellular NiAl-Mo as a homogeneous material, the difference between the largest geometric features, i.e., cell lengths of about $1000\,\mu$m, and the smallest geometric features, i.e., the soft cell boundaries with a thickness around $10\,\mu$m, is still very large. Both memory and runtime limit the size of volume elements which are feasible for computation. Thus, it is imperative to identify both a suitable volume element size and an appropriate resolution, while keeping the possible error of the material response reasonably small [40].

In this context, it is useful to recall some insights from the study on representative volume elements by Kanit et al. [41]. When computing an effective material property based on a randomly generated microstructure of finite size, Kanit et al. [41] identify two sources of error. For an ensemble of finite microstructure realizations of the same size, there will be some scatter in the effective properties of each realization. The difference between the effective property of a single realization and the mean of an infinitely large ensemble is called dispersion or random error. The dispersion can either be reduced by increasing the size of the microstructure or by averaging over multiple microstructures. The second error source is the bias or systematic error, describing the difference between the mean effective properties for a finite volume element size and the effective properties of the infinite volume limit. For instance, choosing a small volume element may induce anomalies in the microstructure leading to incorrect effective properties, independent of the number of realizations considered. Indeed, the systematic error can only be reduced by increasing the size of the microstructure. As the size of the volume element is a limiting factor for the simulations, we aim to identify the smallest microstructure which sufficiently reduces the systematic error and keep track of the dispersion by considering multiple realizations

In the following, we investigate microstructures with varying lengths L and cross-section widths W. For each size, ten volume elements are generated and the effective creep rates for a uniaxial stress loading of 200 MPa in growth direction are computed. Based on preliminary investigations, the voxel size is fixed at $8\,\mu$m, unless stated otherwise. In Fig. 6, we plot the resulting mean values together with the two-sided 99% confidence interval based on Student's $t-$distribution, following Schneider et al. [42]. Note that for better readability, we use a linear scale on the y-axis instead of the typical logarithmic scale when plotting experimental creep rates.

First, we take a look at microstructures of varying width for a fixed length of $L = 2000\,\mu$m. We observe that up to a width of $800\,\mu$m the averaged creep rate increases linearly and subsequently stagnates, see Fig. 6(a). Indeed, the creep rate for $W = 400\,\mu$m is 30% below the stationary level, indicating a large bias. Between $W = 800\,\mu$m and $W = 1200\,\mu$m, the fluctuation of the mean creep rates is small compared to the confidence intervals, revealing that the dispersion is the primary error source. As expected, the confidence intervals narrow down with increasing size. However, when considering an ensemble of ten volume elements, a width of $W = 800\,\mu$m appears sufficient.

Qualitatively, the same trends emerge for volume elements of varying length, see Fig. 6(b). Using microstructures with $L = 1000\,\mu$m, i.e., a single cell length, leads to a systematic underestimation of the creep rate by about 70%. Notably, owing to the imposed regularity of the structure (each cell borders itself in length direction), the dispersion is comparatively small for this case, demonstrating that

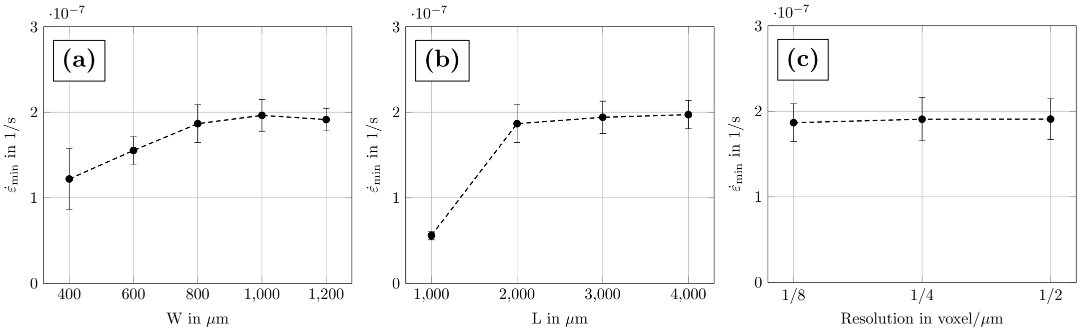

Figure 6: Influence of cell size and resolution on the effective creep rate with default values of $L = 2000\,\mu$m, $W = 800\,\mu$m and a default voxel size of $8\,\mu$m: (a) $\dot{\varepsilon}_{\min}$ vs W; (b) $\dot{\varepsilon}_{\min}$ vs L; (c) $\dot{\varepsilon}_{\min}$ vs resolution

bias and dispersion do not always follow the same trends. For volume elements longer than $2000\,\mu$m, there are only marginal changes in the average creep rates. Overall, we conclude that a length of $2000\,\mu$m, i.e., two cell lengths, is sufficient for our purposes, arriving at a default volume element size of $2000\,\mu\text{m} \times 800\,\mu\text{m} \times 800\,\mu$m for our subsequent investigations. We emphasize that this choice is only safe if an ensemble of (at least) 10 microstructures is considered. As the dispersion is still rather high, with a relative sample standard deviation of 11.5%, using only a single volume element may lead to significant (and undetectable) errors [42]. Further note that these results only hold for investigating the effective creep rate. When studying other physical properties, the representative volume size has to be identified anew.

Last but not least, we validate our chosen resolution for our final volume element size of $L = 2000\,\mu$m and $W = 800\,\mu$m. To this end, the full ensemble of 10 microstructures was discretized with voxel lengths ranging from $2\,\mu$m to $8\,\mu$m. In comparison to the size of volume element, the impact of the resolution is miniscule, see Fig. 6(c). Note that a resolution of $8\,\mu$m is rather coarse, i.e., the soft cell boundary in the discretized microstructure is only one to two voxels in thickness. Hence, the low impact of resolution on the overall accuracy may appear surprising. We found that a key factor for the consistency of the results with respect to resolution stems from in the microstructure generation process, see Sec. 3. For each sampled resolution, the target volume fraction of $\phi = 85\%$ was reached to high accuracy by iteratively thresholding the underlying level-set. Downsampling from a high-resolution microstructure, for instance, by using the median value, produces larger scatter in both volume fraction and creep rate. Overall, continuing the investigation with a default resolution of 8μm per voxel seems reasonable.

4.3 On the definition of the soft cell boundary

In their experimental study on cellular NiAl-Mo, Seemüller et al. [13] observed a massive loss of creep resistance compared to the well-aligned material. More precisely, for a certain nominal stress, the strain-rate differed by about two to three orders of magnitude. The magnitude of this difference was unexpected, as fiber-free boundary regions only accounted for $\sim 15\%$ of the total volume and grain boundaries were generally found to have no effect on the creep resistance of binary NiAl [26]. Hence, we are interested in computationally investigating the loss of creep resistance in the cellular material and comparing our results to the experimental data by Seemüller et al. [13]. In this context, we note that the definition of the soft regions and the volume fraction of the remaining well-aligned material is crucial.

For their estimated cell fraction of 82%-85%, Seemüller et al. [13] only classified completely fiber-free regions as soft regions, see the violet shading in Fig. 7(a). However, larger regions with a coarse fiber

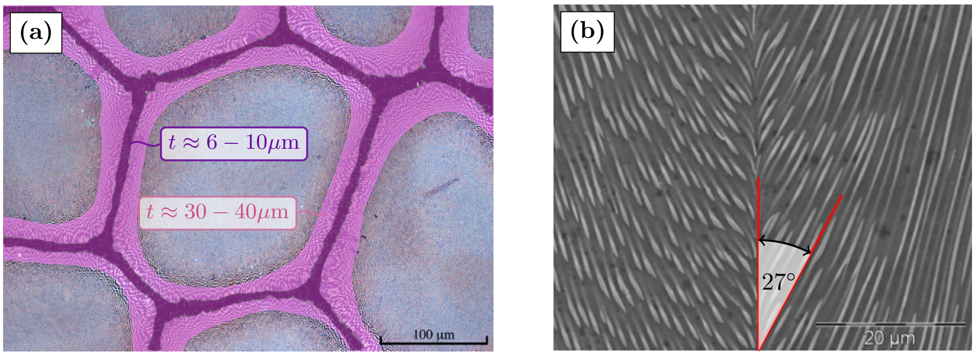

Figure 7: (a) Optical microscopy image by Seemüller et al. [13] with fiber-free (violet) and degenerated (pink) regions; (b) SEM image of boundary region with misaligned fibers by Haenschke et al. [7][2]

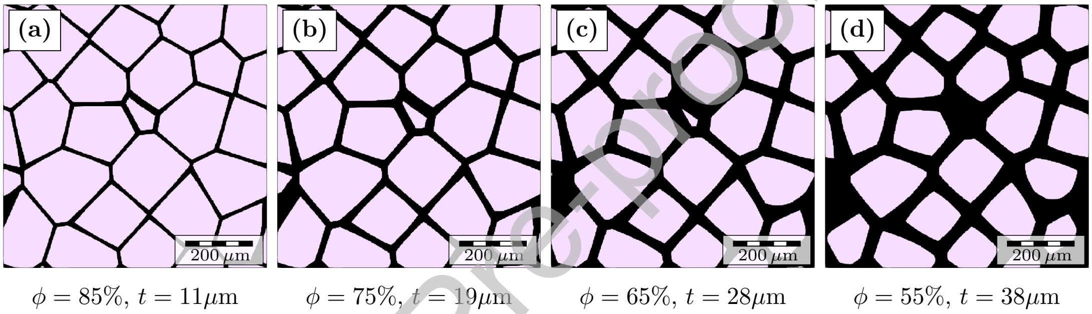

$\phi = 85\%$, $t = 11\mu$m $\phi = 75\%$, $t = 19\mu$m $\phi = 65\%$, $t = 28\mu$m $\phi = 55\%$, $t = 38\mu$m

Figure 8: Artificial microstructures with varying volume fraction ϕ and corresponding boundary width t

distribution and pronounced fiber misalignment can be identified around the cell boundaries (pink shading in Fig. 7(a)). In light of the results in Sec. 2.1, it is plausible that the degenerated regions do not significantly contribute to the creep resistance in growth direction. Indeed, scanning electron microscopy (SEM) images by Haenschke et al. [7] reveal fiber misalignments between 20° to 30° at cell boundaries, see Fig. 7(b). At these angles of misalignment, a single colony of well-aligned NiAl-Mo displays essentially the same creep behavior as the pure NiAl matrix. Thus, it appears reasonable to classify both the fiber-free and the degenerated regions as soft regions. To check this assertion, we consider the simulated creep behavior for varying volume fractions of the hard phase, see Fig. 8(a) - Fig. 8(d) for an example of a microstructure with varying cell distance t and volume fraction ϕ. Comparing the computed creep rates to the data by Seemüller et al. [13] reveals that the experimentally determined creep rates lie between the simulation results for volume fractions of $\phi = 55\%$ and $\phi = 65\%$, see Fig. 9. The cell distance of $28\,\mu\text{m} - 38\,\mu\text{m}$ for the associated synthetic structures roughly matches the thickness of $30\,\mu\text{m} - 40\,\mu\text{m}$ for the coarse region in the microscopy image by Seemüller et al. [13]. Thus, the creep simulations strengthen the hypothesis, that both coarse and fiber-free regions should be classified as soft regions.

Our results highlight that, in contrast to binary NiAl [26], the boundary of the cellular colonies is essential for explaining the overall creep behavior of the cellular material. Owing to its much lower creep resistance,

---

[2] Fig. 7(a) from Seemüller et al. [13] is reused under the STM permissions guidelines: `https://www.stm-assoc.org/intellectual-property/permissions/permissions-guidelines/`. The shading of the boundary regions and the associated annotations have been added. Fig. 7(b) from Haenschke et al. [7] is reused under the CC BY 4.0 license: `https://creativecommons.org/licenses/by/4.0/legalcode`. The visualization for the angle of misalignment has been added.

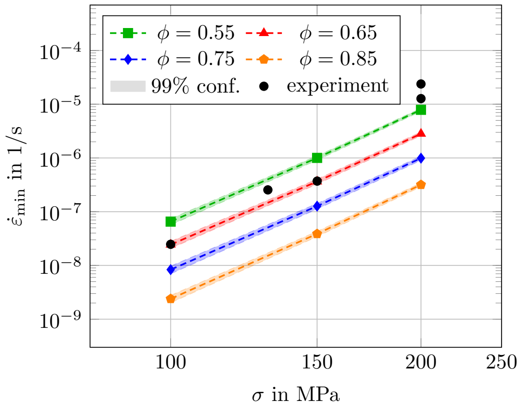

Figure 9: Norton plot for various volume fractions and comparison to experimental data by Seemüller et al. [13]

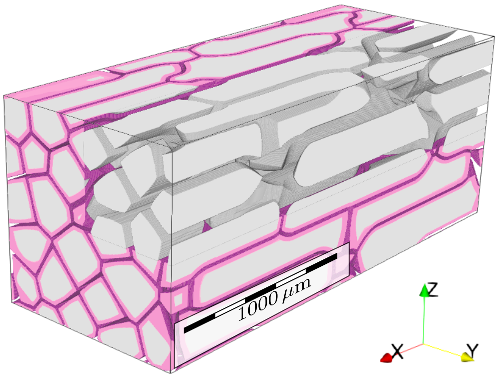

Figure 10: Comparison of reinforcing cell structure between synthetic volume elements with $\phi = 85\%$ and $\phi = 55\%$, difference shaded in pink

properly defining the soft regions and their volume fraction is key for reaching accurate predictions. In particular, identifying the coarse regions with degenerated fiber structure as part of the soft regions sheds light on the deterioration of the creep resistance in cellular NiAl-Mo samples. Compared to the completely fiber-free regions, the degenerated part of the cell boundary occupies two to three times as much volume. Hence, the fraction of the actual hard regions is much lower than the 85% estimated by Seemüller et al. [13], leading to the pronounced loss of creep resistance. An illustration of the difference in reinforcing structure is shown in Fig. 10, where the difference in synthetic volume elements with $\phi = 85\%$ and $\phi = 55\%$, i.e., the impact of the coarse boundary, is visualized. Thus, it appears mandatory to pay special attention on such mesoscale deviations from the ideal fiber morphology when comparing the magnitudes of creep resistance of NiAl-based composites from different experimental datasets. As many alloys in the NiAl-(Cr,Mo) system exhibit similar colony structures with degenerated regions at the cell boundaries [14], these findings should be taken into account when modeling and evaluating the creep resistance. In particular, more complex alloys with a larger number of constituents will be even more prone to form degenerated regions due to extended solidification intervals.

4.4 Influence of the morphology on the overall creep response

In terms of the mechanical properties of directionally solidified NiAl-Mo, aiming for a well-aligned microstructure appears to be optimal. However, this degree of fiber alignment is only achieved under specific processing conditions, i.e., slow growth rates and high temperature gradients, which are typically restricted to a laboratory environment [3, 43, 44]. In contrast, samples solidified in industrial scale furnaces are prone to microstructural irregularities [43]. Hence, for the practical application of NiAl-Mo on a component scale, a robust prediction of the creep behavior in terms of the microstructure morphology is required to find a suitable compromise between mechanical behavior and favorable processing conditions. However, in practice, deliberate morphology modification of NiAl-Mo is limited due to strongly interrelating solidification and processing parameters. Thus, thoroughly characterizing the impact of the morphology on the creep behavior solely based on experiments is difficult.

The level-set framework outlined in Sec. 3 provides greater flexibility for adjusting the aspect ratio and volume fractions of the generated synthetic microstructures. Hence, we expand upon the computations of Sec. 4.3 and investigate the impact of these morphological quantities on the effective creep rate. In addition, we compare our results with the Kelly-Street model [45], which is popular for predicting the microstructure-dependent creep behavior of cellular and fibrous composites and evaluating experimental data [9,13], to assess its accuracy for the case of NiAl-Mo. To this end, we generate microstructures with volume fractions from $55\% - 85\%$ and aspect ratios of $5 - 40$. Aspect ratios higher than the original ratio of 5 were realized by increasing the length of the cellular inclusions and the overall volume elements as part of the microstructure generation routine. Based on the results for $l/d = 5$, see Sec. 4.2, we set the width of all volume elements to four times the width of the cellular inclusions and the length to twice the cell length.

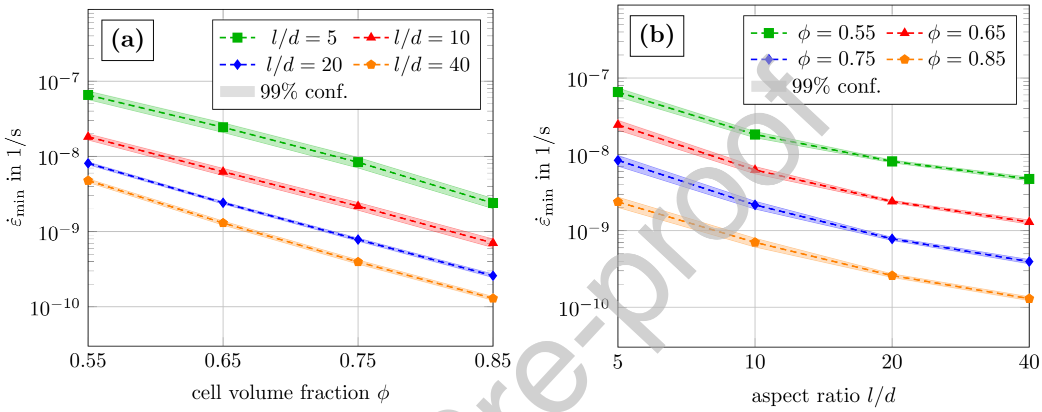

Figure 11: Influence of volume fraction ϕ and aspect ratio l/d on the creep rate of cellular NiAl-Mo for a fixed stress loading of $\sigma = 100\,\text{MPa}$: (a) $\dot{\varepsilon}_{\min}$ vs ϕ; (b) $\dot{\varepsilon}_{\min}$ vs l/d

The minimum creep rates obtained from simulations on the generated microstructures with a fixed stress loading of $\sigma = 100\,\text{MPa}$ are shown in Fig. 11. Recall that, according to Kanit et al. [41], the dispersion of the effective properties is a decent measure for the representativeness of the volume element size. For the cellular microstructures considered in this study, this was confirmed in Sec. 4.2 for volume elements of sufficient length. As a general trend, the dispersion in the effective creep rates decreases with increasing aspect ratio, see Fig. 11. Hence, it is reasonable to assume that the size of the volume elements with an aspect ratio beyond the initial choice of $l/d = 5$ is sufficiently representative as well. In Fig. 11(a), we observe that, for a fixed aspect ratio, a decrease in volume fraction by 20% leads to an increase in creep rate by roughly an order of magnitude. This trend is independent of the specific aspect ratio, as all plots in Fig. 11(a) feature a similar slope. Similarly, for a fixed volume fraction, all plots in Fig. 11(b) exhibit approximately the same general tendency. The creep rate decreases by a factor of about three from $l/d = 5$ to $l/d = 10$. For each subsequent doubling of l/d, the impact of the aspect ratio diminishes. The influence of volume fraction ϕ and aspect ratio l/d on the apparent stress exponent is illustrated in Fig. 12. In particular, all plots in Fig. 12(a) feature the same slope, revealing that the apparent stress exponent is virtually independent of ϕ. In contrast, increasing the aspect ratio leads to a marked change from matrix-controlled creep with $m \approx 6$ for $l/d = 5$ to fiber-controlled creep with $m \approx 9$ for $l/d = 40$, see Fig. 12(b). Due to the change in the apparent stress exponent, the impact of the aspect ratio on the creep rate diminishes further at higher stresses. Note that the observed values for m are inside the range reported in the experimental literature [8–10,13]. Hence the morphology of the colonies arises as another possible source for the scatter in experimental data, again emphasizing that information on the

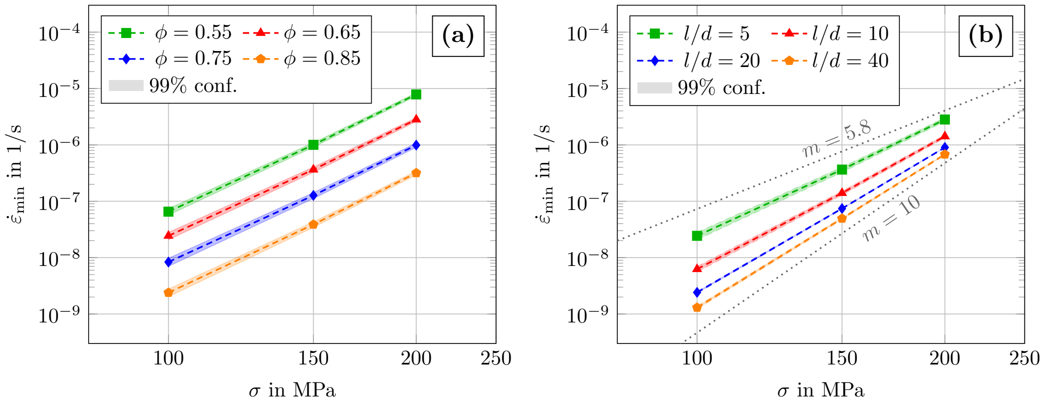

Figure 12: Influence of volume fraction ϕ and aspect ratio l/d on the apparent stress exponent of cellular NiAl-Mo: Norton plots for (a) variable ϕ with $l/d = 5$ and (b) variable l/d with $\phi = 65\%$

mesostructural properties are crucial for a proper assessment of data from different sources.

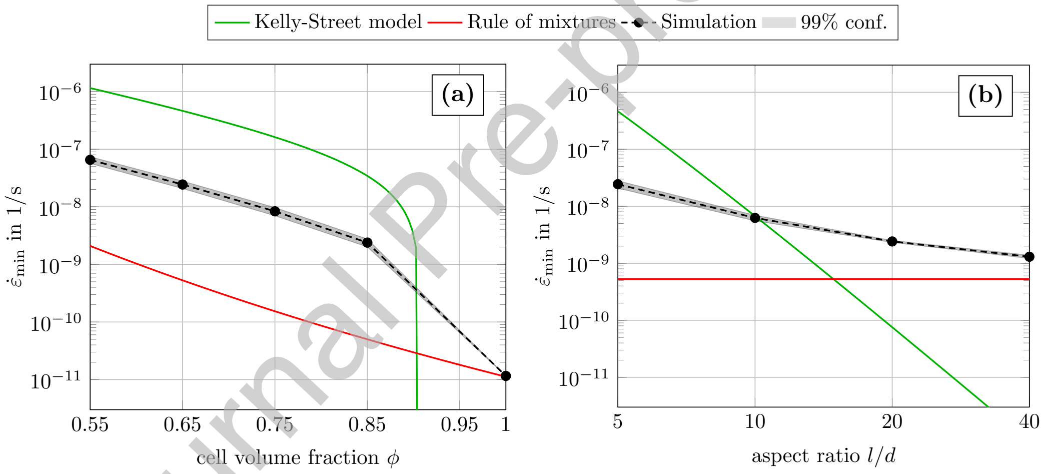

Figure 13: Comparison of the Kelly-Street model [45] to simulation results for $\sigma = 100$MPa: (a) $\dot{\varepsilon}_{\min}$ vs ϕ for $l/d = 5$; (b) $\dot{\varepsilon}_{\min}$ vs l/d for $\phi = 65\%$

Lastly, we turn to the comparison of the simulations to the 1-dimensional shear-lag model by Kelly and Street [45], widely used in materials science to assess and interpret experimental creep data of composites [9,13,46]. In particular, the Kelly-Street model for quasi-rigid inclusions admits a closed-form expression for the creep rate of the composite as a function of the applied stress. Assuming a power-law formulation

$$\dot{\varepsilon} = \dot{\varepsilon}_0^{\text{matrix}} \left(\frac{\sigma}{\sigma_0^{\text{matrix}}} \right)^m \tag{4.1}$$

for the matrix, the creep rate for the composite reads

$$\dot{\varepsilon} = \dot{\varepsilon}_0^{\text{matrix}} \left[\frac{\sigma}{\sigma_0^{\text{matrix}} \left(\Phi(l/d)^{(m+1)/m} - 1 \right) \phi + \sigma_0^{\text{matrix}}} \right]^m \tag{4.2}$$

with the stress transfer function

$$\Phi = \left(\frac{2}{3}\right)^{1/m} \left(\frac{m}{2m+1}\right) \left(\frac{m}{m+1}\right) \left(\sqrt{\frac{\pi}{2\sqrt{3}\phi}} - 1\right)^{-1/m}, \tag{4.3}$$

see Kelly-Street [45, Sec. 3.1] and the modifications by Chan [46]. Note that, in this context, all considered quantities, such as stress σ and strain rate $\dot{\varepsilon}$, are scalar valued. In addition to the Kelly-Street model, we consider the rule of mixtures as a lower bound on the creep rate

$$\sigma = (1-\phi)\,\sigma_0^{\text{matrix}} \left(\frac{\dot{\varepsilon}}{\dot{\varepsilon}_0^{\text{matrix}}}\right)^{1/m} + \phi\,\sigma_0^{\text{fiber}} \left(\frac{\dot{\varepsilon}}{\dot{\varepsilon}_0^{\text{fiber}}}\right)^{1/n}, \tag{4.4}$$

where it is assumed that the fibers are governed by a power-law, analogously to (4.1). Note that the rule of mixtures admits no closed-form solution for the strain rate $\dot{\varepsilon}$ and has to be solved numerically for given stress σ. The material parameters of matrix and well-aligned colonies for the analytical models are listed in Tab. 3.

Soft regions (matrix)	$\dot{\varepsilon}_0^{\text{matrix}} = 1/\text{s}$	$\sigma_0^{\text{matrix}} = 503\,\text{MPa}$	$m = 5.8$
Hard regions (inclusion)	$\dot{\varepsilon}_0^{\text{fiber}} = 1/\text{s}$	$\sigma_0^{\text{fiber}} = 1245\,\text{MPa}$	$n = 10$

Table 3: Parameters for the 1-dimensional power-law model

In Fig. 13(a), we compare the dependency of the creep rate on the cell volume fraction for the original aspect ratio of $l/d = 5$. As an additional data point, we consider the creep rate of the well-aligned material for $\phi = 100\%$. For volume fractions smaller than 85%, the plots of the analytical models and the simulations have a similar slope. However, the Kelly-Street model overestimates the effective creep rate by an order of magnitude compared to the simulation results, which lie roughly at the geometric mean between the Kelly-Street model and the rule of mixtures. In addition, the creep rate for the Kelly-Street model degenerates at $\phi = \pi/2\sqrt{3}$, i.e., the maximum volume fraction for a hexagonal packing of continuous fibers as assumed by Kelly-Street [45]. The results highlight that using the Kelly-Street model beyond its intended regime may lead to inaccurate predictions. Indeed, Kelly-Street note that their theory may be inaccurate for small l/d [45] and validate their model for $l/d = 50$ and $l/d = 100$ [47]. Keeping in mind that the Kelly-Street model assumes a constant strain rate in the matrix and zero strain rate in the fibers, the origins of the model inaccuracy may be traced to the heterogeneity of the local fields. In Fig. 14 the strain rate in growth direction is visualized for $l/d = 5$. Note that, for the purpose of portraying the fields, we choose a higher resolution of $4\,\mu$m per voxel.

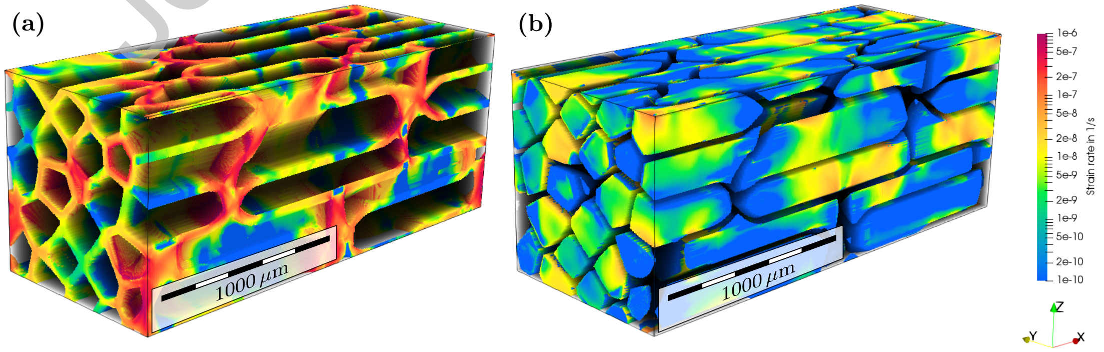

Figure 14: Strain rate component in growth direction for a microstructure with aspect ratio $l/d = 5$ and volume fraction $\phi = 65\%$: (a) Boundary network; (b) Cellular inclusions

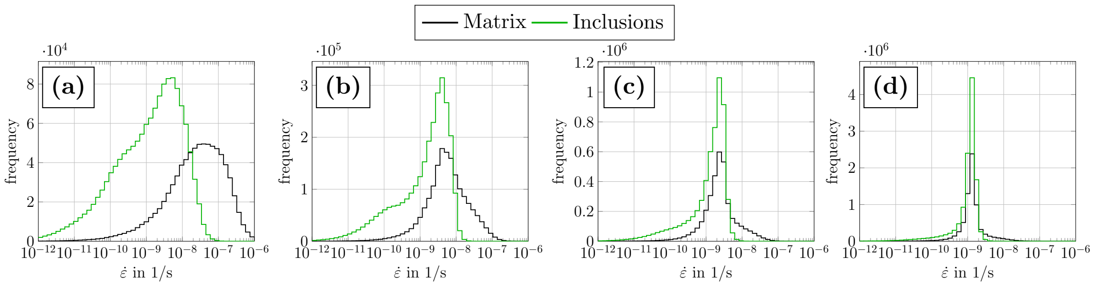

$l/d = 5$ $l/d = 10$ $l/d = 20$ $l/d = 40$

Figure 15: Histograms of the strain-rate in growth direction for various aspect ratios

Evidently, the strain rate in both cellular inclusions and matrix is strongly heterogeneous for this case, see Fig. 15(a) for the corresponding histogram. Thus, it is not surprising that the Kelly-Street model struggles to arrive at accurate predictions. With increasing aspect ratio, the strain-rate field becomes more homogeneous, see Fig. 15(a)-Fig. 15(d), and the simulated creep rates approach the results for the rule of mixtures. However, for high l/d, the assumption of zero strain-rate in the fibers leads to a vast underestimation of the effective creep rate of the composite by the Kelly-Street model, see Fig. 13(b). Thus, we conclude that the model should be confined to cases where the inclusions are truly rigid.

5 Conclusions

The present work was devoted to studying the creep behavior of directionally solidified NiAl-Mo eutectics with a cellular mesostructure using FFT-based micromechanics solvers. Our conclusions are as following:

- Combining the level level-set framework for microstructure generation [1, 20, 21] with FFT-based solvers [15] proves to be a flexible approach for simulating the creep response of cellular materials. In particular, the suggested procedure enables the individual control of morphological parameters such as cell volume fraction and aspect ratio. As alloys with a larger number of constituents in the NiAl-(Cr,Mo) system may be even more prone to developing microstructural irregularities, a flexible simulation tool-set is crucial for assessing their creep response.
- Simulations on both well-aligned and cellular material strongly suggest that the degenerated regions with high fiber misalignment do not substantially contribute to the overall creep strength of NiAl-Mo. As a result, the identified fraction of the hard regions was significantly lower than first estimated by Seemüller et al. [13]. This offers an explanation for the rather large decrease in creep resistance compared to the well-aligned material, which was found to be surprising at that time.
- Studying the impact of morphology on the creep behavior of cellular NiAl-Mo, we observed that the volume fraction of the hard regions has a strong influence on the (minimum) creep rate, irrespective of the aspect ratio of the cells. The aspect ratio primarily determines the apparent stress exponent, i.e., if the creep behavior is matrix-controlled or fiber-controlled. Hence, information on the mesostructure is crucial for comparing experimental creep data from different sources.
- In contrast to Seemüller et al. [13], we found that the shear-lag model by Kelly-Street [45] for quasi-rigid fibers was not able to accurately describe the creep behavior of cellular NiAl-Mo. The finite creep resistance of the inclusions, their relatively low aspect ratio and the resulting inhomogeneity

of the microscopic strain-rate field were identified as main error sources. Furthermore, based on its geometric assumptions, the Kelly-Street model breaks down for cell volume fractions above 90%. Overall, the results demonstrate that the basic assumptions and scope of the model need to be carefully considered, when it is used for interpreting experimental data. The Kelly-Street model for creeping fibers [45, Sec. 3.2] may serve as a starting point for developing analytical models which address the aforementioned limitations.

Acknowledgements

The authors D. Wicht and A. Kauffmann gratefully acknowledge the financial support by the Helmholtz Association of German Research Centers under the framework of the Helmholtz Research School on “Integrated Materials Development for Novel High Temperature Alloys (IMD)”, Grant No. VH-KO-610. M. Schneider was supported by by the German Research Foundation (DFG) within the International Research Training Group “Integrated engineering of continuous-discontinuous long fiber reinforced polymer structures“ (GRK 2078). M. Heilmaier and T. Böhlke acknowledge the financial support by the Karlsruhe Institute of Technology (KIT) within the EXU funding “KIT Future Fields”, Grant ACDC.

CRediT author statement

Daniel Wicht: Investigation, Methodology, Software, Visualization, Writing - Original Draft
Alexander Kauffmann: Conceptualization, Visualization, Writing - Review & Editing
Matti Schneider: Supervision, Software, Writing - Review & Editing
Martin Heilmaier: Conceptualization, Funding acquisition, Writing - Review & Editing
Thomas Böhlke: Conceptualization, Supervision, Resources, Funding acquisition, Writing - Review & Editing

A Remarks on computing the DN_k level sets on voxel images

A.1 Using Euclidean distance transforms to compute level sets

In the following, we briefly lay out how Euclidean distance transforms (EDTs), which are standard algorithms in image processing [48], may be exploited for computing the DN_k level-sets on voxel images. Suppose a binary microstructure image $\mathcal{I} : \Omega \rightarrow \{0, 1\}$ is given on a discretized domain $\Omega = \{0, ..., N\}^3$, with a set of inclusion voxels Φ (typically with value 1) and matrix voxels $\Phi^c = \Omega \backslash \Phi$ (typically with value 0). For any image with a marked set of object voxels $\mathcal{O}$, an EDT assigns to each voxel the distance to its nearest object voxel. Thus, the signed distance field DN_1 of $\mathcal{I}$ may be computed by a three-step process:

1. Identify the boundary voxels $\partial\Phi$ of the inclusions [49, Sec 9.5]. For our implementation, we check the connectivity based on the 6-neighbourhood, i.e., voxels are connected if they share a face.
2. Compute the EDT with the boundary $\partial\Phi$ as object $\mathcal{O}$.
3. Assign a negative sign to the distance for all voxels inside Φ.

For computing the nearest neighbour level sets DN_k of higher order, the sequential updating strategy by Sonon et al. [20, Sec. 2.4.1] may be used. To this end, the subsets Φ_i of all particles, with $\Phi = \bigcup_{i=1}^{n} \Phi_i$, have to be identified in a pre-processing step, using a connected-component extraction algorithm [49, Sec 9.5]. For each particle, firstly, its signed distance field DS_{Φ_i} is computed by applying the outlined three-step process to Φ_i. Secondly, the DN_k fields are updated according to Sonon [20, Sec. 2.4.1]

$$\begin{aligned} DN_k &\leftarrow \max(DN_{k-1}, \min(DN_k, DS_{\Phi_i})) \\ DN_1 &\leftarrow \min(DN_1, DS_{\Phi_i}), \end{aligned} \tag{A.1}$$

starting with $k_{\max}$, i.e., the highest desired value of k. Note, that the computational effort for this generic strategy is proportional to the number of particles in the image $\mathcal{I}$. However, certain EDTs may be modified to evaluate DN_k in a single pass as shown in the next section.

A.2 Choice of EDT algorithm

For an extensive performance comparison and discussion of various EDTs for 2-dimensional images, we refer to the study by Fabbri et al. [48]. Following their taxonomy, EDTs may be broadly categorized into scanning algorithms and propagating algorithms [48], differing in the order in which the voxels are processed. For the present discussion, we consider one representative algorithm of each family.

In scanning algorithms, the image is processed in terms of its rows, columns and planes. The fastest EDT in this category [48] is the algorithm by Meijster et al. [31], which exploits that the minimization problem for computing the square Euclidean distance transform may be solved for each spatial dimension separately. The algorithm lends itself well to parallelization and periodicity of the image can be incorporated at virtually no additional cost, using the scheme of Coeurjolly [50].

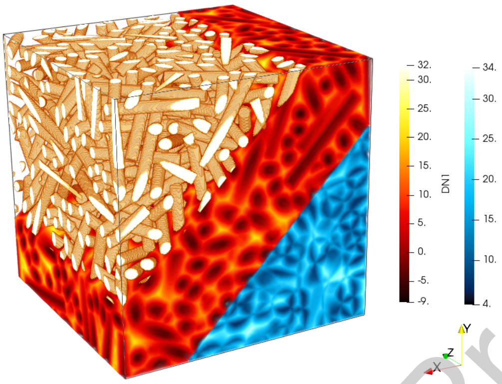

Figure 16: Overview of the microstructure and the DN_1 (red scale) and DN_2 (blue scale) level sets for a structure with 500 fibers

Propagating algorithms update the distance field in a narrow band or wavefront, emanating from the object voxels. As Dijkstra-type algorithms they are very similar to the fast marching method for solving the (related but more general) eikonal equation. Algorithms of this type [51–53] mostly differ in details such as the data structure for the wavefront or the propagated information, see Sec. 7.4.1. in Fabbri et al. [48] for a generic description. For our implementation, we choose the algorithm by Lotufo et al. [53] using a bucket queue as data structure and propagating the nearest object voxel. The bucket queue enables a partial parallelization of the algorithm. Periodicity is integrated by considering the periodic 6-neighbourhood during propagation. Note that propagation-type algorithms are generally not exact, see Cuisenaire-Macq [52] for a detailed discussion of the 2-dimensional case. However, in our studies the maximum error for computing DN_1 was usually below a single voxel length, which we consider acceptable.

As a first benchmark, we investigate the performance of the algorithms for computing the DN_1 level set of a microstructure generated with the SAM algorithm by Schneider [30], featuring 500 isotropically distributed fibers with an aspect ratio of 10, occupying a volume fraction of 23.5%, see Fig. 16. All EDT benchmarks were performed on a desktop computer with an Intel i7-8700K CPU using 6 threads. The runtimes for different spatial discretizations from 64^3 voxels up to 512^3 voxels are shown in Fig. 17(a). For the chosen structure, both EDT algorithms exhibit linear time complexity with respect to the voxel count. However, the scanning algorithm is more than an order of magnitude faster than the propagating algorithm, confirming the trends observed by Fabbri et al. [48] in the 3-dimensional setting.

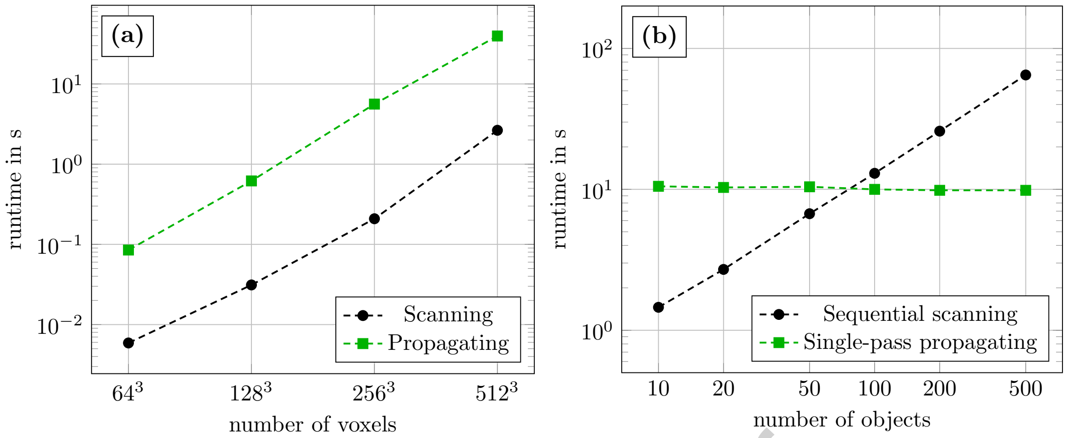

Figure 17: Benchmark of the scanning EDT by Meijster et al. [31] and the propagating EDT by Lotufo et al. [53] (and its modified version Alg. 1) for computing the nearest neighbour level sets of isotropically packed fiber structures: (a) Computing DN_1 for varying voxel counts; (b) Computing DN_1 and DN_2 for varying fiber counts

The vast difference in performance may suggest that this is the end of the story and the scanning algorithm by Meijster et al. [31] is clearly superior. However, the situation changes when considering level sets DN_k of higher order. As far as the authors are aware, the scanning algorithm is limited to the sequential updating strategy (A.1) outlined in the last section. Thus, the runtime for computing the DN_k level sets becomes dependent on the number of inclusions. This is illustrated in Fig. 17(b), where the runtimes for computing DN_1 and DN_2 for microstructures with a fixed voxel count of 256^3 and a varying number of packed fibers are plotted.

On the other hand, the propagating algorithm by Lotufo et al. [53] can be naturally modified to compute the DN_k level sets up to a maximum level $k_{\max}$ in a single pass. A pseudocode for the modified algorithm is outlined in Alg. 1. Informally speaking, a unique label is assigned to each object and the associated emanating wavefront. By allowing wavefronts with different labels to pass through each other, the order of arrival at a certain coordinate determines the level k of DN_k. At the end, all points are visited $k_{\max}$ times. Note that a similar concept for fast marching algorithms was outlined in Sonon's thesis [20, Sec. 2.4.1]. The performance of the resulting single-pass propagating algorithm is virtually independent of the number of inclusions, see Fig. 17(b). In particular, it becomes the preferable option for object counts larger than 100. At the end, some closing remarks are in order:

1. Due to the limited size of feasible volume elements for cellular NiAl-Mo, see Sec. 4.2, we did not exceed fiber counts of 100 during the microstructure generation process. Thus, the scanning algorithm of Meijster et al. [31] was used for the present study. However, the propagating scheme in Alg. 1 is more suitable as a general-purpose method.

2. The sequential scanning algorithm may compute the level sets for higher $k_{\max}$ at little additional cost, as the updating step (A.1) is usually less expensive than computing the level set of a single particle. On the other hand, the computational effort for the single-pass propagating algorithm increases notably, as more voxels need to be processed. Thus, at higher $k_{\max}$ the break-even point in terms of inclusion count may shift to higher numbers in favor of the scanning algorithm. However, for the most common morphing operations [1, 20, 21] the necessary $k_{\max}$ does not exceed 3. Hence,

our evaluation of the algorithms is not substantially affected.

3. If a sequential evaluation of the level sets is unavoidable, e.g., as part of the LS-RSA microstructure generation process by Sonon et al. [1], then Meijster's algorithm [31] is the method of choice. Due to its high efficiency for computing the level set of a single particle, it relieves the user of using pre-screening strategies [1]. In addition, using Coeurjolly's approach [50] avoids the creation and consideration of periodic neighbours.

Algorithm 1 Propagation algorithm for computing DN_k in a single pass

Auxiliaries:

- A voxel object v stores its associated coordinates $v.x$, a label $v.label$, a root voxel $v.root$ and the periodic square distance to its root $v.dsquare$
- Q is a queue for storing voxels, ordered by their square distance
- $\mathcal{I}_{\text{labeled}}(x)$ is an array with the same structure as $\mathcal{I}$ but the coordinates of each object Φ_i are marked with a unique integer label
- $N(x)$ returns the voxels with coordinates of the periodic neighbourhood of point x
- $V(x)$ is an array, storing the number of wavefronts, which have passed point x
- $DN(x,k)$ is an array, storing the value of the DN_k level set at point x
- $L(x,k)$ is an array storing the label of the kth wavefront which has passed x

Input: Binary image $\mathcal{I}$, maximum depth $k_{\max}$

Output: Level sets $DN(x,k)$

```
Initialize $V$, $DN$ and $L$ to 0
Extract particles $\Phi_i$, assign an integer label $\geq 1$ to each particle and initialize $\mathcal{I}_{\text{labeled}}(x)$
Identify the particle boundaries $\partial\Phi_i$
Add all points in $\partial\Phi_i$ with their associated label and themselves as root to $Q$
while $Q$ is not empty do
    Remove voxel $v$ with smallest $v.dsquare$ from $Q$
    if $V(v.x) < k_{\max}$ and $v.label \notin \{L(v.x,0),...,L(v.x,k_{\max})\}$ then
        $L(v.x, V(v.x)) \leftarrow v.label$
        $d \leftarrow \sqrt{v.dsquare}$
        if $v.label = \mathcal{I}_{\text{labeled}}(v.x)$ then
            $d \leftarrow -d$
        end if
        $DN(v.x, V(v.x)) \leftarrow d$
        $V(v.x) \leftarrow V(v.x) + 1$
        for each $n \in N(v.x)$ do
            if $V(n.x) < k_{\max}$ and $v.label \notin \{L(n.x,0),...,L(n.x,k_{\max})\}$ then
                $n.root \leftarrow v.root$
                $n.label \leftarrow v.label$
                $n.dsquare \leftarrow \|n.x - n.root.x\|^2$
                Add $n$ to $Q$
            end if
        end for
    end if
end while
```

References

[1] B. Sonon, B. François, and T. J. Massart, “A unified level set based methodology for fast generation of complex microstructural multi-phase RVEs,” Computer Methods in Applied Mechanics and Engineering, vol. 223–224, pp. 103–122, 2012.

[2] R. D. Noebe, R. R. Bowman, and M. V. Nathal, “Physical and mechanical properties of the B2 compound NiAl,” International Materials Reviews, vol. 38, no. 4, pp. 193–232, 1993.

[3] H. Bei and E. P. George, “Microstructures and mechanical properties of a directionally solidified NiAl–Mo eutectic alloy,” Acta Materialia, vol. 53, no. 1, pp. 69–77, 2005.

[4] H. Bei, S. Shim, G. M. Pharr, and E. P. George, “Effects of pre-strain on the compressive stress-strain response of Mo-alloy single-crystal micropillars,” Acta Materialia, vol. 56, pp. 4762–4770, 2008.

[5] P. Sudharshan Phani, K. E. Johanns, G. Duscher, A. Gali, E. P. George, and G. M. Pharr, “Scanning transmission electron microscope observations of defects in as-grown and pre-strained Mo alloy fibers,” Acta Materialia, vol. 59, no. 5, pp. 2172–2179, 2011.

[6] H. Bei, S. Shim, E. P. George, M. K. Miller, E. G. Herbert, and G. M. Pharr, “Compressive strengths of molybdenum alloy micro-pillars prepared using a new technique,” Scripta Materialia, vol. 57, no. 5, pp. 397–400, 2007.

[7] T. Haenschke, A. Gali, M. Heilmaier, M. Krüger, H. Bei, and E. P. George, “Synthesis and characterization of lamellar and fibre-reinforced NiAl-Mo and NiAl-Cr,” Journal of Physics: Conference Series, vol. 240, p. 012063, 2010.

[8] M. Dudová, K. Kuchařová, T. Barták, H. Bei, E. P. George, C. Somsen, and A. Dlouhý, “Creep in directionally solidified NiAl–Mo eutectics,” Scripta Materialia, vol. 65, no. 8, pp. 699–702, 2011.

[9] L. Hu, G. Zhang, W. Hu, G. Gottstein, S. Bogner, and A. Bührig-Polaczek, “Tensile creep of directionally solidified NiAl–9Mo in situ composites,” Acta Materialia, vol. 61, no. 19, pp. 7155–7165, 2013.

[10] J. Albiez, I. Sprenger, C. Seemüller, D. Weygand, M. Heilmaier, and T. Böhlke, “Physically motivated model for creep of directionally solidified eutectics evaluated for the intermetallic NiAl–9Mo,” Acta Materialia, vol. 110, pp. 377–385, 2016.

[11] J. Albiez, H. Erdle, D. Weygand, and T. Böhlke, “A gradient plasticity creep model accounting for slip transfer/activation at interfaces evaluated for the intermetallic NiAl-9Mo,” International Journal of Plasticity, vol. 113, pp. 291–311, 2019.

[12] A. Misra, Z. L. Wu, M. T. Kush, and R. Gibala, “Deformation and fracture behaviour of directionally solidified NiAl-Mo and NiAl-Mo(Re) eutectic composites,” Philosophical Magazine A, vol. 78, no. 3, pp. 533–550, 1998.

[13] C. Seemüller, M. Heilmaier, T. Haenschke, H. Bei, A. Dlouhý, and E. P. George, “Influence of fiber alignment on creep in directionally solidified NiAl-10Mo in-situ composites,” Intermetallics, vol. 35, pp. 110–115, 2013.

[14] C. Gombola, A. Kauffmann, G. Geramifard, M. Blankenburg, and M. Heilmaier, “Microstructural investigations of novel high temperature alloys based on NiAl-(Cr,Mo),” Metals, vol. 10, no. 7, p. 961, 2020.

[15] H. Moulinec and P. Suquet, “A numerical method for computing the overall response of nonlinear composites with complex microstructure,” Computer Methods in Applied Mechanics and Engineering, vol. 157, pp. 69–94, 1998.

[16] B. Burgarella, A. Maurel-Pantel, N. Lahellec, J.-L. Bouvard, N. Billon, H. Moulinec, and F. Lebon, “Effective viscoelastic behavior of short fibers composites using virtual DMA experiments,” Mechanics of Time-Dependent Materials, vol. 23, pp. 337–360, 2019.

[17] D. Wang, P. Shantraj, H. Springer, and D. Raabe, “Particle-induced damage in Fe–TiB_2 high stiffness metal matrix-composite steels,” Materials and Design, vol. 160, pp. 557–571, 2018.

[18] R. A. Lebensohn, A. K. Kanjarla, and P. Eisenlohr, “An elasto-viscoplastic formulation based on fast Fourier transforms for the prediction of micromechanical fields in polycrystalline materials,” International Journal of Plasticity, vol. 32-33, pp. 59–69, 2012.

[19] P. Eisenlohr, M. Diehl, R. A. Lebensohn, and F. Roters, “A spectral method solution to crystal elasto-viscoplasticity at finite strains,” International Journal of Plasticity, vol. 46, pp. 37–53, 2013.

[20] B. Sonon, On advanced techniques for generation and discretization of the microstructure of complex heterogeneous materials. PhD thesis, Université Libre de Bruxelles, 2014.

[21] B. Sonon, B. François, and T. J. Massart, “An advanced approach for the generation of complex cellular material representative volume elements using distance fields and level sets,” Computational Mechanics, vol. 56, no. 2, pp. 221–242, 2015.

[22] J. F. W. Bishop, “A theoretical investigation of the plastic deformation of crystals by glide,” Philosophical Magazine, vol. 44, pp. 51–64, 1953.

[23] J. W. Hutchinson, “Bounds and self-consistent estimates for creep of polycrystalline materials,” Proceedings of the Royal Society of London A, vol. 348, pp. 101–127, 1976.

[24] R. A. Lebensohn, C. S. Hartley, C. N. Tomé, and O. Castelnau, “Modeling the mechanical response of polycrystals deforming by climb and glide,” Philosophical Magazine, vol. 90, no. 5, pp. 567–583, 2010.

[25] D. Wicht, M. Schneider, and T. Böhlke, “An efficient solution scheme for small-strain crystal-elasto-viscoplasticity in a dual framework,” Computer Methods in Applied Mechanics and Engineering, vol. 358, p. 112611, 2020.

[26] J. D. Whittenberger, “Effect of composition and grain size on slow plastic flow properties of NiAl between 1200 and 1400 K,” Journal of Materials Science, vol. 22, no. 2, pp. 394–402, 1987.

[27] S. Williams and A. Philipse, “Random packings of spheres and spherocylinders simulated by mechanical contraction,” Physical Review E, vol. 67, pp. 1–9, 2003.

[28] K. Naumenko and H. Altenbach, “A phenomenological model for anisotropic creep in a multipass weld metal,” Archive of Applied Mechanics, vol. 74, no. 11, pp. 808–819, 2005.

[29] T. J. Massart, B. Sonon, K. E. M. Kamel, L. H. Poh, and G. Sun, “Level set-based generation of representative volume elements for the damage analysis of irregular masonry,” Meccanica, vol. 53, no. 7, pp. 1737–1755, 2018.

[30] M. Schneider, “The sequential addition and migration method to generate representative volume elements for the homogenization of short fiber reinforced plastics,” Computational Mechanics, vol. 59, no. 2, pp. 247–263, 2017.

[31] A. Meijster, J. B. T. M. Roerdink, and W. H. Hesselink, “A General Algorithm for Computing Distance Transforms in Linear Time,” in Mathematical Morphology and its applications to image and signal processing (J. Goutsias, L. Vincent, and D. S. Bloomberg, eds.), Boston: Springer, 2002.

[32] G. W. Milton, The Theory of Composites. Cambridge: Cambridge University Press, 2002.

[33] D. Wicht, M. Schneider, and T. Böhlke, “On Quasi-Newton methods in FFT-based micromechanics,” International Journal for Numerical Methods in Engineering, vol. 121, no. 8, pp. 1665–1694, 2020.

[34] M. Schneider, F. Ospald, and M. Kabel, “Computational homogenization of elasticity on a staggered grid,” International Journal for Numerical Methods in Engineering, vol. 105, no. 9, pp. 693–720, 2016.

[35] M. Schneider, “A review of nonlinear FFT-based computational homogenization methods,” Acta Mechanica, 2021.

[36] J. Segurado, R. A. Lebensohn, and J. LLorca, “Chapter One - Computational Homogenization of Polycrystals,” Advances in Applied Mechanics, vol. 51, pp. 1–114, 2018.

[37] R. A. Lebensohn and A. D. Rollett, “Spectral methods for full-field micromechanical modelling of polycrystalline material,” Computational Materials Science, vol. 173, p. 109336, 2020.

[38] M. Kabel, S. Fliegener, and M. Schneider, “Mixed boundary conditions for FFT-based homogenization at finite strains,” Computational Mechanics, vol. 57, no. 2, pp. 193–210, 2016.

[39] M. Schneider, D. Wicht, and T. Böhlke, “On polarization-based schemes for the FFT-based computational homogenization of inelastic materials,” Computational Mechanics, pp. 1–23, 2019.

[40] A. Gote, A. Fischer, C. Zhang, and B. Eidel, “Computational Homogenization of Concrete in the Cyber Size-Resolution-Discretization (SRD) Parameter Space,” arxiv e-prints, vol. 2103.08957, pp. 1–30, 2021.

[41] T. Kanit, S. Forest, I. Galliet, V. Mounoury, and D. Jeulin, “Determination of the size of the representative volume element for random composites: statistical and numerical approach,” International Journal of Solids and Structures, vol. 40, no. 13–14, pp. 3647–3679, 2003.

[42] M. Schneider, M. Josien, and F. Otto, “Representative volume elements for matrix-inclusion composites - a computational study on periodizing the ensemble,” submitted, 2021.

[43] S. Bogner, L. Hu, S. Hollad, W. Hu, G. Gottstein, and A. Bührig-Polaczek, “Microstructure of a eutectic NiAl-Mo alloy directionally solidified using an industrial scale and a laboratory scale Bridgman furnace,” International Journal of Materials Research, vol. 103, no. 1, pp. 17–23, 2012.

[44] L. Hu, W. Hu, G. Gottstein, S. Bogner, S. Hollad, and A. Bührig-Polaczek, “Investigation into microstructure and mechanical properties of NiAl-Mo composites produced by directional solidification,” Materials Science and Engineering A, vol. 539, pp. 211–222, 2012.

[45] A. Kelly and K. N. Street, “Creep of discontinuous fibre composites II. Theory for the steady-state,” Proceedings of the Royal Society of London A, vol. 328, no. 1573, pp. 283–293, 1972.

[46] K. S. Chan, “Modeling creep behavior of niobium silicide in-situ composites,” Materials Science and Engineering: A, vol. 337, no. 1–2, pp. 59–66, 2002.

[47] A. Kelly and K. N. Street, “Creep of discontinuous fibre composites I. Experimental behaviour of lead-phosphor bronze,” Proceedings of the Royal Society of London A, vol. 328, no. 1573, pp. 267–282, 1972.

[48] R. Fabbri, L. D. F. Costa, J. C. Torelli, and O. M. Bruno, “2D Euclidean Distance Transform Algorithms: A Comparative Survey,” ACM Computing Surveys, vol. 40, no. 1, pp. 1–44, 2008.

[49] R. C. Gonzalez and R. E. Woods, Digital Image Processing. New York: Pearson, 4th ed., 2018.

[50] D. Coeurjolly, “Distance Transformation , Reverse Distance Transformation and Discrete Medial Axis on Toric Spaces,” in 19th International Conference on Pattern Recognition, pp. 1–4, 2008.

[51] I. Ragnemalm, “Neighborhoods for Distance Transformations Using Ordered Propagation,” CVGIP: Image Understanding, vol. 56, no. 3, pp. 399–409, 1992.

[52] O. Cuisenaire and B. Macq, “Fast Euclidean Distance Transformation by Propagation Using Multiple Neighborhoods,” Computer Vision and Image Understanding, vol. 76, no. 2, pp. 163–172, 1999.

[53] R. A. Lotufo, A. A. Falcao, and F. A. Zampirolli, “Fast Euclidean Distance Transform using a Graph-Search Algorithm,” Proceedings 13th Brazilian Symposium on Computer Graphics and Image Processing, pp. 269–275, 2000.

eclaration

Declaration of interests

☒ The authors declare that they have no known competing financial interests or personal relationships that could have appeared to influence the work reported in this paper.

☐The authors declare the following financial interests/personal relationships which may be considered as potential competing interests: